Author Manuscript

Author Manuscript

Author Manuscript

Author Manuscript

HHS Public Access

Author manuscript

Neuroimage. Author manuscript; available in PMC 2020 September 11.

Published in final edited form as:

Neuroimage. 2020 September ; 218: 116978. doi:10.1016/j.neuroimage.2020.116978.

Morphology of perivascular spaces and enclosed blood vessels in young to middle-aged healthy adults at 7T: Dependences on age, brain region, and breathing gas

Xiaopeng Zong[a,b,*], **Chunfeng Lian**[a,b], **Jordan Jimenez**[a], **Koji Yamashita**[a,b], **Dinggang Shen**[a,b], **Weili Lin**[a,b]

[a]Biomedical Research Imaging Center, Chapel Hill, NC, USA

[b]Department of Radiology, University of North Carolina at Chapel Hill, Chapel Hill, NC, USA

Abstract

Perivascular spaces (PVSs) are fluid-filled spaces surrounding penetrating blood vessels in the brain and are an integral pathway of the glymphatic system. A PVS and the enclosed blood vessel are commonly visualized as a single vessel-like complex (denoted as PVSV) in high-resolution MRI images. Quantitative characterization of the PVSV morphology in MRI images in healthy subjects may serve as a reference for detecting disease related PVS and/or blood vessel alterations in patients with brain diseases.

To this end, we evaluated the age dependences, spatial heterogeneities, and dynamic properties of PVSV morphological features in 45 healthy subjects (21–55 years old), using an ultra-high-resolution three-dimensional transverse relaxation time weighted MRI sequence ($0.41 \times 0.41 \times 0.4$ mm^3) at 7T. Quantitative PVSV parameters, including apparent diameter, count, volume fraction (VF), and relative contrast to noise ratio (rCNR) were calculated in the white matter and subcortical structures. Dynamic changes were induced by carbogen breathing which are known to induce vasodilation and increase the blood oxygenation level in the brain.

PVSV count and VF significantly increased with age in basal ganglia (BG), so did rCNR in BG, midbrain, and white matter (WM). Apparent PVSV diameter also showed a positive association with age in the three brain regions, although it did not reach statistical significance. The PVSV VF and count showed large inter-subject variations, with coefficients of variation ranging from 0.17 to 0.74 after regressing out age and gender effects. Both apparent diameter and VF exhibited significant spatial heterogeneity, which cannot be explained solely by radio-frequency field inhomogeneities. Carbogen breathing significantly increased VF in BG and WM, and rCNR in thalamus, BG, and WM compared to air breathing.

This is an open access article under the CC BY-NC-ND license (http://creativecommons.org/licenses/by-nc-nd/4.0/).

[*]Corresponding author. Department of Radiology and Biomedical Research Imaging Center, University of North Carolina at Chapel Hill, CB#7515, Chapel Hill, NC, 27599, USA. xiaopeng_zong@med.unc.edu (X. Zong).

CRediT authorship contribution statement

Xiaopeng Zong: Conceptualization, Project administration, Methodology, Software, Formal analysis, Writing - original draft. **Chunfeng Lian:** Software. **Jordan Jimenez:** Project administration, Writing - review & editing. **Koji Yamashita:** Formal analysis. **Dinggang Shen:** Resources. **Weili Lin:** Conceptualization, Writing - review & editing, Supervision, Funding acquisition.

Author Manuscript Author Manuscript Author Manuscript Author Manuscript

Our results are consistent with gradual dilation of PVSs with age in healthy adults. The PVSV morphology exhibited spatial heterogeneity and large inter-subject variations and changed during carbogen breathing compared to air breathing.

Keywords

Perivascular spaces; Aging; High field MRI; Carbogen breathing; Human brain; Heterogeneity; Morphology; Glymphatic system

1. Introduction

Perivascular spaces (PVSs) are fluid-filled spaces surrounding penetrating arteries (PAs) or veins (Zhang et al., 1990). They are an essential pathway of the brain's glymphatic system which plays an important role in clearing metabolic wastes from the brain (Iliff et al., 2012; Rasmussen et al., 2018). Increased number of MRI-visible PVSs has been widely reported in patients compared to healthy controls, including those with Alzheimer's disease (Boespflug et al., 2018b; Cai et al., 2015; Chen et al., 2011; Hansen et al., 2015), multiple sclerosis (Kilsdonk et al., 2015; Wuerfel et al., 2008), traumatic brain injury (TBI) (Inglese et al., 2005), small vessel disease (SVD) (Doubal et al., 2010; Duperron et al., 2018; Zhu et al., 2010), stroke (Park et al., 2019a), and sleep disturbance (Opel et al., 2019; Song et al., 2017), suggesting that the diseased conditions can lead to enlargement of PVSs. In addition to association with current diseases, higher numbers of PVSs were also associated with increased *risks* of future SVD (Ding et al., 2017), stroke (Duperron et al., 2019; Gutierrez et al., 2017), recurrence of transient ischemic attack (Lau et al.,2017), cognitive decline (Ding et al., 2017; Park et al., 2019b), and development of subdural fluid accumulation in mild TBI patients (Koo et al., 2019), suggesting that PVS imaging may have potential prognostic values.

Many possible mechanisms have been proposed to explain PVS enlargement, including neuroinflammation (Aribisala et al., 2014; Wuerfel et al., 2008), brain atrophy (Awad et al., 1986; Heier et al., 1989), blood brain barrier (BBB) leakage (Benhaïem-Sigaux et al., 1987; Poirier et al., 1983), blockage of fluid drainage from the PVS (Derouesné et al., 1987; Homeyeret al., 1996; Pollock et al., 1997), and coiling of PAs (Brown et al., 2002; Hughes, 1965).

Because of the limited spatial resolution of MRI, PVSs and enclosed bloodvessels (typical diameter < 100 μm (Adachietal., 1998)) cannot be resolved in most cases and appear as single vessel like structures in MRI images. Therefore, we will refer to such structures as PVS/blood Vessel complexes (PVSVs) throughout the paper. The distinction between PVS and PVSV becomes more important at higher spatial resolution, as higher spatial resolution allows visualization of smaller PVSVs in which the PVS contribution to the MR signal of the PVSVs decreases.

In addition to associations with diseases, increased number of MR-visible PVSVs with increasing age has also been reported in healthy participants (Feldman et al., 2018; Inglese et al., 2005; Wuerfel et al., 2008). One plausible explanation for the increased incidents of

Author Manuscript Author Manuscript Author Manuscript Author Manuscript

visible PVSVs may be normal aging related processes affecting the whole brain. However, some other recent studies reported no age-related changes in elderly healthy subjects using 3T and 7T high-resolution MRI (voxel size ≤ 1 × 1 × 1 mm^3) (Boespflug et al., 2018a; Bouvy et al., 2016), suggesting that the dilation of PVSVs may only occur in a small fraction of PVSVs and thus reflect potentially pathological processes in local brain regions. Therefore, further studies are needed to further clarify the age dependence of the PVSVs.

Leveraging the increased signal to noise ratio at 7T, we have previously demonstrated that large numbers (~500) of PVSVs can be visualized in young healthy subjects using ultra-high-resolution transverse relaxation time (T_2) weighted (T_2w) MRI (Zong et al., 2016). Furthermore, we have developed a deep learning based segmentation method to facilitate automatic delineation of the PVSVs (Lian et al., 2018), allowing more detailed and quantitative characterization of their morphological features. In this study, we report detailed characterization of PVSV morphology in 37 neurologically normal subjects aged between 21 and 55 years using the above-mentioned sequence and image analysis method. We hypothesize that the increased spatial resolution and the quantitative approach will provide more statistical power for detecting age related changes in these subjects.

Earlier studies have only focused on PVSV alterations under chronical conditions. Therefore, it remains unclear whether the PVSV morphology varies with acute changes in physiological condition, such as sleep vs wakefulness and different breathing gases. To investigate acute PVSV morphology changes, we carried out MRI scans under both air and carbogen breathing conditions, the latter is known to induce robust flow and oxygenation increases in the blood (Liu et al., 2019). Furthermore, the oxygenation in the PVS fluid may also increase because of diffusion of dissolved oxygen into the PVS and subarachnoid space (Mehemed et al., 2014; Zaharchuk et al., 2005). Based on the known effects of the oxygenation on longitudinal relaxation time (T_1) and T_2 (Grgac et al., 2013; Li and van Zijl, 2020), we hypothesize that these changes will result in increased PVSV signal under our experimental condition and potentially lead to the detection of more PVSV voxels compared to air breathing.

2. Materials and methods

2.1. Subjects

This study was approved by the institutional review board of the University of North Carolina at Chapel Hill. The inclusion criteria were as follows: (a) no history of hypertension or diabetes mellitus, (b) no history of cerebrovascular diseases, (c) age between 21 and 55 years old, and (d) not pregnant or breast-feeding. A total of 46 volunteers (35 females) who met the above inclusion criteria were recruited. Informed consents were obtained from all subjects prior to scanning. All acquired T_2w images were evaluated for the presence of white matter (WM) hyperintensities (WMH) and subjects excluded if WMH were found.

Author Manuscript Author Manuscript Author Manuscript Author Manuscript

2.2. Data acquisition

All images were acquired using a 7T MRI scanner (Siemens Healthi- neer, Erlangen, Germany) equipped with a Nova 32-channel receiver and 8-channel transmitter head coil (Nova Medical, Wilmington, MA, USA). No radio frequency magnetic field (B_1) shimming was performed. The amplitude scales of all the transmitter channels were set to one and their phase offsets were determined by the manufacture's automatic process which assessed the RF phases relative to one receiver channel.

A 3D variable flip angle turbo spin echo (TSE) sequence was used to image PVSVs (Busse et al., 2006; Zong et al., 2016). The sequence parameters were as follows: TR/TE = 3000/326 ms, partial Fourier factor = 0.79 and 0.625 along the phase encoding and partition encoding directions, respectively, GRAPPA factor = 3 along phase encoding direction, the ratio of pseudo-steady state to thermal equilibrium magnetizations = 0.45 and T_1/T_2 = 3500/600 ms for calculating variable flip angles, FOV = 210 × 210 × 99.2 mm^3, matrix size = 512 × 512 × 248, voxel size = 0.41 × 0.41 × 0.4 mm^3, scan time = 8:03 min. The echo spacing was 3.74 ms and the echo train had 187 echoes with all ky = 0 lines acquired at the 87th echo. Note that the TR was shorter than previously (Zong et al., 2016) used (TR = 5 s) to shorten the scan time and the TE was in the range of 204–473 ms where the contrast was found to be ≥ 90% of the peak contrast in simulation.

Since older subjects could be more prone to head motion, leading to experimental confounds for evaluating PVSV age effects (Savalia et al., 2017), 3D fat navigator images (Gallichan et al., 2016) were acquired within each TR to monitor head motion. The navigator images had a voxel size = 2.2 × 2.2 × 2.2 mm^3 and were acquired during the idle period of the TSE sequence. The RF frequency was centered at 3.4 ppm up-field from water. The sequence parameters were: TR/TE = 3.1/1.5 ms, flip angle = 7°, GRAPPA factors = 4 × 4, FOV = 220 × 220 × 180 mm^3, matrix size = 100 × 100 × 82, voxel size = 2.2 × 2.2 × 2.2 mm^3, partial Fourier factor = 0.75 along both the phase and partition encoding directions. In addition, a transmitter B_1 ($B_{1,t}$) mapping sequence based on a slice-selective pre-saturation pulse followed by gradient echo readout was performed for studying the potential effect of $B_{1,t}$ inhomogeneity on the measured PVSV spatial distribution. $B_{1,t}$ maps were calculated based on the intensity ratio between images acquired with and without the pre-saturation pulses, respectively. The sequence parameters were: TE = 1.89 ms, TR = 8 s, voxel size = 3.1 × 3.1 mm^2, slice thickness = 5 mm, gap between slices = 5 mm, and matrix size = 64 × 64 × 16.

Prior to imaging, subjects were outfitted with a Hudson RCI Medium Concentration-Elongated adult face mask (CNA Medical, Royse City, TX, USA). The TSE scan was first performed while a subject was breathing medical air delivered through the mask. Upon completion of the first scan, the breathing gas was then switched to carbogen (95% of O_2 and 5% of CO_2, Airgas, Radnor, PA, USA) at a flow rate of 20 L/min. The scan was repeated starting at 1.5 min after the gas switch.

2.3. Data analysis

2.3.1. Head motion parameters—The series of navigator images in each subject were registered to the first image in the same series using the 3dvolreg tool in AFNI (Cox, 1996).

Author Manuscript Author Manuscript Author Manuscript Author Manuscript

Motion ranges, defined as the differences of the maximum and minimum values of the six rigid-body motion parameters, were calculated. The rotational and translational motion ranges were then combined by root mean square to obtain the total rotational (M_R) and translational motions (M_T), respectively. M_R and M_T were used as measures of the rotational and translational motions.

2.3.2. Regions of interest (ROIs)—To evaluate the age and breathing gas effects on PVSV morphology, we defined 4 ROIs including the thalamus, basal ganglia (BG), midbrain, and WM in the subject image space. Thalamus, BG, and midbrain were defined based on ROIs defined in the JHU-Eve atlas (Oishi et al., 2008). BG included the caudate nucleus, putamen, and globus pallidus, and midbrain included the midbrain and red nucleus. The WM probability map from the MNIICBM 152 nonlinear atlas was employed to define the WM ROI (Fonov et al., 2011). To register ROIs and probability maps to the subject image space, T_2w images from the atlases were first registered to each subject's T_2w image using Advanced Normalization Tools (ANTs) (Avants et al., 2011). Before the registration, the subjects' images were downsampled by a factor of 2 by skipping every other voxel in all three dimensions to reduce computation time. Skulls were then removed from the downsampled images and the atlas images using the BET tool in FSL (Smith, 2002). The deformation fields from ANTs were applied to transform the ROIs and probability maps from atlases to the downsampled T_2w images, followed by upsampling by a factor of 2 to match the resolution of the original T_2w images. The WM ROIs were defined as voxels with WM probability>0.9. Voxels in the WM ROI that overlapped with the other three ROIs were excluded, which was only 0.38 ± 0.04% of the total WM voxels.

Furthermore, to study the spatial heterogeneity of the PVSV morphology within WM and the spatial relationships between PVSV morphology and arterial territories, four ROIs were defined within the WM according to the territories of the anterior, middle, and posterior cerebral arteries (ACA, MCA, and PCA). First, we adopted the territories defined in (Kim et al., 2019), which was defined on the MNI brain template based on 1160 large artery infarcts. The territory ROIs were derived from Fig. 3 of (Kim et al., 2019) by extracting the colored brain regions. We included all colored voxels with a confidence interval >50%. The images were digitized to a matrix size of 215 × 155 × 12 and voxel size of 1.05 × 1.05 × 6. Since no scale bar was provided in the images, the in-plane voxel size was determined by visually matching the mask with the MNI template T_1 weighted image. The extracted ROIs were modified by removing holes and isolated clusters with less than 20 voxels in each slice. The resulting territory ROIs were resampled to the same voxel size ($1 \times 1 \times 1$ mm^3) as the MNI template image using the 3dresmple tool in AFNI (Cox, 1996). Finally, the watershed (WS) ROI was defined as voxels that belonged to two or all territories. The three territory ROIs were then modified by excluding WS voxels.

The territories defined in (Kim et al., 2019) did not include the inferior and superior parts of the brain. Therefore, a second territory map (Mutsaerts et al., 2015) was adopted to assign voxels not included in (Kim et al., 2019). The map was defined in the same atlas space based on arterial transit times (Mutsaerts et al., 2015). The authors kindly provided the digital mask file. Although ROIs were defined over the whole cerebrum in (Mutsaerts et al., 2015), due to the low ASL signal in WM, they did not cover all WM voxels. Therefore, they were

Author Manuscript Author Manuscript Author Manuscript Author Manuscript

used only to define the ACA, MCA, and PCA territories in slices that were not included in (Kim et al., 2019). Fig. 1 shows the combined territories from the two studies overlaid on the MNI template T_1-weighted image. The combined territories were registered onto the subject image space using ANTs, following the same procedure as described above. Then, voxels from the ACA, MCA, PCA, and WS territories that overlapped with the WM ROI were labelled as WM-ACA, WM-MCA, WM-PCA, and WM-WS, respectively. Only 6.3 ± 0.3% of the WM voxels lied outside the WM-ACA, WM-MCA, and WM-PCA, and WM-WS ROIs.

2.3.3. PVSV morphological parameters—We employed a fully convoluted neural network (Lian et al., 2018) to delineate PVSV masks. The masks were visually inspected by a radiologist (K. Y.) and false PVSV voxels were manually removed. PVSVs were defined as spatially connected clusters in the edited masks that had more than one voxel. A PVSV path was defined for each PVSV cluster and diameter was calculated for each voxel in the PVSV path (VoP). To define the path, Euclidean distances among all pairs of voxels within a PVSV cluster were calculated and the pair with the longest distance were identified. Then the PVSV path was defined as the shortest path connecting the identified voxel pair by travelling across the PVSV voxels, using the graphshortestpath function in MATLAB (Mathworks, Natick, MA, USA). Next, we calculated an apparent diameter (D_{VoP}) for each VoP based on the number of voxels (N_{nearest}) in the PVSV that were closer to that VoP than to any other VoPs:

$$D_{\mathrm{Vop}} = 2\sqrt{N_{nearest} \times V_{\mathrm{voxel}}/(l\pi),} \quad (1)$$

where l was the mean distance to its neighboring VoP(s), and V_{voxel} was the volume of a single voxel. If a PVS voxel had equal closest distances to two VoPs, it would add 0.5 to N_{nearest} to each of the two VoPs.

ROI-averaged apparent PVSV diameter, volume fraction (VF), count, and relative contrast to noise ratio (rCNR) were calculated to study the spatial, age, and breathing gas dependences of PVSV morphology. Mean diameter was calculated by averaging D_{VoP} over all VoPs in an ROI. VF was calculated as the number of PVSV voxels in an ROI divided by the total number of ROI voxels. PVSV count was defined as the number of PVSV clusters that intersected with an ROI. PVSVs that intersected with more than one ROI were assigned to the ROI that contained the most voxels from such PVSVs. rCNR was calculated as the mean contrast between the PVSVs and surrounding tissue divided by the mean image intensity in a background ROI, where the surrounding tissue was defined as the new voxels added when dilating the PVSV mask by one voxel in all three dimensions and the background ROI was drawn as a 15.6 × 15.6 × 15.6 mm^3 cube outside skull at the corner of the field of view. To study the spatial dependence, the ROI-averaged results were calculated in seven ROIs, including thalamus, BG, midbrain, WM-ACA, WM-MCA, WM-PCA, and WM-WS. To study the age and breathing gas dependences, only four ROIs were used by replacing the four WM ROIs with a single WM ROI as defined above to improve statistical power. Only images acquired under air breathing were used for studying the spatial and age dependences.

Author Manuscript Author Manuscript Author Manuscript Author Manuscript

To further evaluate the spatial heterogeneity of PVSV distribution, we calculated a group-averaged VF map in the MNI template space. Only images acquired under the air-breathing condition were used for the calculation. VF was first calculated for each voxel in the subject image space by calculating the fraction of PVSV voxels in a 6 × 6 × 6 cube centered at the voxel. The resulting VF maps were then downsampled by a factor of 2 and transformed to the MNI template space using the inverse deformation fields generated during the above ANTs registration. The transformed maps were then averaged across subjects to obtain the final VF map.

2.3.4. B_{1t} and T_2w image intensities—To evaluate the potential effects of B_1 inhomogeneities on PVSV morphology, we calculated ROI-averaged B_{1t} and T_2w image intensities during air breathing. While B_{1t} only measures B_1 field of the transmitter coils, T_2w image intensity reflects the combined effects of B_{1t} and receiver coil sensitivities. Before calculating ROI averaged results, the B_{1t} maps obtained from the B_1 mapping sequence were normalized by the calibrated nominal B_{1t} values and resampled to the same voxel and matrix sizes as the T_2w images, using the 3dresample program in AFNI. A group averaged B_1t map was generated by warping the resampled B_1t maps onto the MNI template following the same procedure for warping VF maps and averaging the resulting maps over all subjects. To study the potential B_1 contributions to VF heterogeneity within WM, we defined two circular ROIs centered on WM regions with high and low VFs (thus referred to as ROI_{high} and ROI_{low}) on the 101th slice in the MNI atlas and compared the mean VFs, B_{1t} and T_2w image intensities between these two ROIs.

2.3.5. Statistical analyses—To study the age dependence of motion, we calculated the Spearman's correlation coefficients between M_R and M_T and age. Furthermore, we performed Wilcoxon's rank sum tests to compare the motion parameters between male and female participants, and between the air and carbogen breathing conditions. False discovery rate (FDR) correction was used to adjust for multiple comparisons for different motion parameters and gender or gas types. Throughout the paper, corrected p values ≤ 0.05 are considered statistically significant.

To evaluate the age and gender effects on PVSV parameters, linear regression analyses were carried out for the mean diameter, count, VF, rCNR, and ROI volume in the BG, thalamus, midbrain, and WM ROIs with age and gender (male = 1 and female = 0) as independent variables. FDR correction was used to adjust for multiple comparisons in the 4 ROIs. To quantify the degree of inter-subject variations in the PVSV parameters that were independent of age and gender, the residual variance of regression analysis was normalized by the group mean of the corresponding parameter to derive the residual coefficient of variation (COV).

To study the spatial heterogeneities of PVSV parameters and B_1 fields, Welch' s ANOVA tests were performed to compare the mean diameters, counts, VFs, rCNRs, B_{1t}, and image intensities in the seven ROIs. For tests that revealed significant differences, post-hoc Games-Howell tests were performed to identify ROI pairs that exhibited significant differences after correcting for multiple comparison with FDR. Furthermore, Wil- coxon's signed rank tests were performed to compare the VFs, B_{1t}, and image intensities in ROI_{high} and ROI_{low}.

Author Manuscript Author Manuscript Author Manuscript Author Manuscript

To study the effects of breathing gas, only subjects who underwent both the air and carbogen scans were included in the analysis. Wilcoxon's signed rank tests were performed to compare the mean diameters, VFs, counts, and rCNRs under the air and carbogen breathing conditions in BG, thalamus, midbrain, and WM. FDR corrections were performed to correct for multiple comparisons in the four ROIs.

2.4. Simulation

To better understand the effects of carbogen breathing on PVSV morphology, simulations were carried out to compare the signal intensities between the two gas breathing conditions. Carbogen can have several effects on the observed PVSV signal. First, carbon dioxide is a known vasodilator which increases blood flow to brain tissue (Brian, 1998), leading to higher oxygenation fraction of hemoglobin (Y) in penetrating venules and longer venous blood T_2. Second, the high O_2 content in carbogen will increase the partial pressure of dissolved oxygen in arterial blood and PVSs, which leads to shorter T_1 in both the PA and PVS compartments because of the paramagnetic property of dissolved oxygen (Grgac et al., 2013; Tripathi et al., 1984). Oxygen can enter the PVS from the PAs by diffusion and from the subarachnoid space by inflow of the cerebral spinal fluid (CSF), as increased pO_2 in the CSF during 100% O_2 breathing has been reported in earlier studies (Anzai et al., 2004; Mehemed et al., 2014; Zaharchuk et al., 2005).

In our simulation, we assumed Y to be 0.65 in penetrating venules under air breathing and to increase by 0.1 during carbogen breathing (An et al., 2012). pO_2 was assumed to be 114 mmHg and 312 mmHg during air and carbogen breathing, respectively (Anzai et al., 2004). The Severinghaus' human blood O_2 dissociation curve was used to calculate pO_2 in venules and Y in PAs (Severinghaus, 1979). In a previous study, the pO_2 in CSF was increased by 124 mmHg in cortical sulci. However, no pO_2 change was observed in the lateral and third ventricles, suggesting potential partial volume effects from cortical veins (Zaharchuk et al., 2005). Therefore, we assumed a pO2 increase of 62 mmHg (half of 124 mmHg) during carbogen breathing in PVSs. Although this value may not match the true pO_2 change, it will allow us to evaluate the directionality of the MRI intensity change.

We assumed hematocrit fraction (Hct) to be 0.42. Based on known Hct, pO2, and Y, we calculated blood T_1 (in s) as (Grgac et al., 2013)

$$\frac{1}{T_1} = f_{ery}[0.722 + 0.265(1 - Y)] + [0.321 + r(pO_2 - 87)](1 - f_{ery}), \quad (2)$$

where the first and second terms on the right are the contributions from the erythrocytes and plasma, respectively, $r = 1.9 \times 10^{-4}$ s^{-1}/mmHg is the relaxivity of dissolved oxygen, and f_{ery} is the fraction of water in the erythrocytes which is equal to 0.348 for Hct = 0.42. We calculated blood T_2 using a two-compartment exchange model (Li and van Zijl, 2020), which predicts T_2 values based on field strength, Y, Hct, and echo spacing. We set the echo spacing to match our MRI protocol (3.74 ms) and set other model parameters to be the same as those given in Tables 1, 4 and 5 of (Li and van Zijl, 2020). The effect of dissolved O_2 on T_2 relaxation is negligible and not considered (Li and van Zijl, 2020). The T1 and T_2 for the PVSs during air breathing was assumed to be 3500 ms and 600 ms, respectively (Zong et al.,

Author Manuscript Author Manuscript Author Manuscript Author Manuscript

2016). The increases in T_1 and T_2 relaxation rates during carbogen breathing were calculated by assuming O_2 relaxivity to be the same as for blood ($r = 1.9 \times 10^{-4}$ s^{-1}/VmmHg). We used the same relaxivity for T_1 and T_2, since an earlier study found similar T_1 and T_2 relaxivities of O_2 in plasma at 3 T (Ma et al., 2016), consistent with the effects of paramagnetic moments with short correlation times in a solution (Bloembergen and Morgan, 1961). Table 1 lists the resulting pO_2, Y, T_1, and T_2 values in penetrating venules, PAs, and PVSs under both gas conditions.

The TSE signal was simulated with the extended phase diagram algorithm (Hennig, 1988). All sequence parameters were the same as those in the experiment. The MRI image intensity was taken as the simulated signal intensity at the k-space center (87th echo) weighted by the water content which was assumed to be 1 for PVS and 0.845 for blood with Hct = 0.42 (Grgac et al., 2013). For simplicity, the effects of fluid motion were not considered in the simulation.

2.5. Code and data availability

The data and MATLAB code for the study can be provided upon signing a formal data sharing agreement.

3. Results

3.1. Number of subjects

TSE images under air-breathing condition were obtained from all subjects whereas thirty-seven subjects underwent the additional carbogen-breathing scans. Due to technical issues, the navigator images were only acquired in 40 and 33 subjects during the air and carbogen scans, respectively. Images were visually inspected and severe motion artifacts, such as blurring of PVSVs and apparent ripples within WM, were found in 8 and 13 cases during air and carbogen breathing, respectively. These cases were excluded from all subsequent analyses. WMH were absent in all but one female subject who had widespread WMH indicating possible multiple sclerosis. This subject was informed of the imaging finding and also excluded from the analysis. Table 2 lists the total number of subjects in each category. The number of female subjects and the age range in each category are also given.

3.2. Head motion

For subjects with fat navigator images, there were no significant correlations between the motion parameters (i.e. M_R and M_T) and age (Spearman's correlation $p \geq 0.13$) under either air (n = 31) or carbogen-breathing (n = 20) conditions. Table 3 lists the mean M_R and M_T for different gender and gas combinations, and the p values for comparisons between gender and gas conditions. M_T or M_R was not significantly different between air and carbogen scans (corrected $p \geq 0.18$). Female participants (n = 20) had significantly less translational and rotational motion than male (n = 11) participants during air breathing (corrected $p \leq 0.014$). However, there was no gender difference during carbogen breathing (corrected $p \geq 0.57$; 13 female vs 7 male).

Author Manuscript Author Manuscript Author Manuscript Author Manuscript

3.3. Manual editing of PVSV masks

Manually removed false PVSV voxels consisted of hyperintense voxels in the sulci, outside the brain, and in the WM. False PVSV voxels in the WM had lower intensity than neighboring PVSV voxels. An example of the automatic segmentation and manually edited results are shown in Fig. 2. On average, 6.0 ± 3.6% of false PVSV voxels were removed by manual editing. The manual editing took about 20–30 min for each image. After manual editing, the total number of PVS clusters ranged from 451 to 2314 over the whole brain.

3.4. Age and gender dependences

The linear regression analyses (n = 25 female and 12 male) of diameter, count, VF, and rCNR gave positive slopes for the age dependence in most ROIs, as shown in Fig. 3. After FDR correction, the slopes were significantly different from zero for PVSV count ($p = 2.4 \times 10^{-5}$) and VF (p = 0.00034) in BG, and for rCNR in BG (p = 0.037), MB (p = 0.015), and WM (p = 0.031). There was no significant dependence on gender for any of the PVSV parameters. The linear regression coefficients and intercepts are given in Table 4. The ROI volumes showed no significant age dependence in any ROI ($p \geq 0.23$) in the linear regression analyses.

After regressing out the age and gender effects, the PVSV VF and count still showed large inter-subject variations in thalamus, midbrain, and WM, as shown by the large residual COV (≥32%) in Table 5. Table 5 also lists the total variances (R-square) explained by linear regression, which only accounted for ≤46% of the total variances in all ROIs.

3.5. Spatial heterogeneities

The group averaged VF map exhibited a high degree of heterogeneity, as shown in Fig. 4. VF is the highest near the posterior inferior part of BG and the sub-insula region (denoted by the blue arrows), second highest in WM-ACA and WM-MCA territories, and lowest in thalamus, midbrain, and WM-PCA territories. For quantitative comparisons, group averaged diameters, VFs, and rCNRs in the seven ROIs are shown in Fig. 5. All three parameters were significantly different among the ROIs (Welch ANOVA test, $p \leq 1.1 \times 10^{-25}$, n = 37). Based on the post-hoc Games-Howell tests (n = 37), diameter was significantly larger in BG than in the other regions (corrected $p \leq 1.8 \times 10^{-5}$) and was lowest in the WM-PCA among the four WM ROIs (corrected $p \leq 0.001$). VF was significantly higher in BG, WM-ACA, and WM-MCA than in the remaining ROIs (corrected $p < 0.05$) and was lowest in WM-PCA among the WM ROIs (corrected $p \leq 4.6 \times 10^{-8}$). Compared to the WM-ACA and WM-MCA, VF in WM-PCA was 78 ± 12 to 79 ± 11% lower. rCNR was higher in BG and midbrain than in the other ROIs (corrected $p \leq 4.5 \times 10^{-7}$). There was no significant difference in rCNR among the 4 WM regions (corrected $p \geq 0.55$).

The group averaged B_{1t} map in Fig. 6 shows that B_{1t} was highest near the center of the brain and decreased towards the peripheral. The mean B_{1t} and image intensities in different ROIs are shown in Fig. 7, which shows clear B_{1t} and image intensity differences among the ROIs (Welch- ANOVA test, $p \leq 4.7 \times 10^{-55}$, n = 37). Based on the post-hoc Games- Howell tests (n = 37), $B_{1,t}$ was the strongest in thalamus and midbrain (corrected $p \leq 2.8 \times 10^{-6}$), and 18 ± 4% to 39 ± 9% higher in BG than in the WM ROIs (corrected $p \leq 2.0 \times 10^{-10}$). Among the

Author Manuscript Author Manuscript Author Manuscript Author Manuscript

WM ROIs, $B_{1,t}$ was 12 ± 2% to 18 ± 8% higher in WM-ACA than the other three WM ROIs (corrected $p \leq 2.2 \times 10^{-6}$). On the other hand, image intensities were significantly higher in WM than non-WM ROIs (corrected $p \leq 0.01$). Among the WM ROIs, the intensity was 16 ± 4% to 18 ± 5% lower in WM-PCA than in WM-ACA, WM-MCA, and WM-WS (corrected $p \leq 1.3 \times 10^{-7}$).

The 13th slice in Fig. 4 shows the locations of the manually drawn ROI_{low} and ROI_{high} in WM which had low and high VFs, respectively. The group averaged VF in ROI_{low} was significantly lower than that in ROI_{high} (0.02 ± 0.08% vs 1.9 ± 2.2%, $p = 4.5 \times 10^{-7}$, signed rank test, n = 37). On the other hand, the image intensities in the ROI_{low} and ROI_{high} were almost identical (35.2 ± 3.6 vs 34.9 ± 4.4, p = 0.46, signed rank test, n = 37), while $B_{1,t}$ was significantly higher in ROI_{low} than in ROI_{high} (0.87 ± 0.08 vs 0.74 ± 0.06, $p = 1.1 \times 10^{-7}$, signed rank test, n = 37).

3.6. Dependence on breathing gas

Fig. 8 compares the mean diameters, VFs, counts, and rCNRs in thalamus, BG, midbrain, and WM between the air and carbogen breathing conditions. Compared to air breathing, carbogen breathing increased apparent PVSV diameter in WM (signed rank test, corrected p = 0.006, n = 22), and VF in BG and WM (corrected $p \leq 0.003$), while no significant difference in PVSV count was observed in any ROI. Consistent with the diameter and VF increases, increased rCNRs were observed in thalamus, BG, and WM (corrected $p \leq 0.001$). Table 6 lists the group averaged (n = 22) diameter, VF, count, rCNR, their percent differences between carbogen and air, and p values in each ROI.

The simulated signal intensities for the penetrating venules, PAs, and PVSs are given in the last two columns of Table 1. Consistent with the observed rCNRs difference between the carbogen and air breathing conditions, the intensity is higher during carbogen breathing in all three compartments. The relative change is the largest in the venules, while it has the lowest intensity among the three compartments due to its shortest T_2.

4. Discussion

Using ultra-high-resolution MRI at 7T, we studied (1) the age- dependences of PVSV morphology in young to middle-aged healthy adults, (2) the inter-subject and spatial variations of PVSV morphology, and (3) the changes of the PVSV parameters under carbogen breathing. We found that PVSV volume fraction, count, and rCNR significantly increased with age in BG, so did rCNR in midbrain and WM. Apparent PVSV diameter also showed positive correlation with age in BG, midbrain, and WM, although it did not reach statistical significance. The VF and apparent diameter were spatially heterogeneous, and VF and count showed large inter-subject variations. Furthermore, we found that carbogen breathing significantly increased the apparent diameter, VF, and rCNR in BG, thalamus, and WM (see Fig. 8).

4.1. Partial volume effects on PVSV age-dependence

Despite the high spatial resolution adopted in the study, partial volume effects were still present in the PVSV voxels since the outer diameter of normal PVSs in putamen in subjects

Author Manuscript Author Manuscript Author Manuscript Author Manuscript

of 62–90 years old are in the range of 0.13–0.96 mm, with the majority below 0.5 mm (Pesce and Carli, 1988). Similar diameter range are expected in other brain regions. The significantly increased rCNR with age in BG, midbrain, and WM is consistent with gradual dilation of PVSs with age which reduces the partial volume fraction of non-PVS compartments in PVSV voxels, leading to increased signal intensity and rCNR because of the much longer T_2 of PVS fluid. The increased rCNR would allow more PVSV voxels to be correctly identified by the segmentation algorithm at older age, consistent with the significantly increased VF and count with age in BG. WM also showed a trend of increased VF and count with age, although they did not reach statistical significance. Furthermore, a trend of increased diameter with age was observed in BG, midbrain, and WM.

4.2. Possible mechanisms of age-related PVS dilation

Among the various mechanisms described in the Introduction, brain atrophy and coiling of blood vessels may have contributed to PVS dilation with age, while the relevance of the other mechanisms (neuroinflammation, BBB leakage, blockage of fluid flow) are less clear. Shrinkage of adult brain with age has been widely reported (Bishop et al., 2017; DeCarli et al., 2005; Good et al., 2001; Kruggel, 2006; Smith et al., 2007). However, there were mixed results for the volume-age relationships for WM and subcortical gray matter regions. The WM volume either exhibited slight linear decreases (rate ~ 0.001–0.1%/y but not significant) (Kruggel, 2006; Smith et al., 2007), or had an inverted-U shape with a peak at ~45 years of age (Fjell et al., 2009; Good et al., 2001; Grieve et al., 2005; Inano et al., 2013; Narvacan et al., 2017). Similarly, different volume age relationships have been reported for the subcortical gray matter structures (Tullo et al., 2019). Nevertheless, most studies reported decreased BG and thalamus volumes with age between 21 and 55 years (Bishop et al., 2017; Fjell et al., 2009; Goodro et al., 2012; Inano et al., 2013; Narvacan et al., 2017; Potvin et al., 2016) with a rate of ~0.3%/y (Bishop et al., 2017; Goodro et al., 2012). In our study, only BG showed significant PVSV VF increase with age at a rate of 0.029%/y which is much less than the rate of 0.3%/y (Bishop et al., 2017; Goodro et al., 2012), consistent with the expectation that the intracranial spaces vacated by atrophy are only partially occupied by PVSVs and only a fraction of the PVSVs in the brain are visualized. In addition to brain atrophy, aging is associated with complex macrostructural and micro- structural remodeling of brain vasculature (Xu et al., 2017), resulting in increased tortuosity of PAs (Brown et al., 2002; Spangler et al., 1994; Thore et al., 2007). The constant pounding and tugging of the pulsating coiled PAs may provide a driving force for the expansion of pia membrane lining the PVSs (Hughes, 1965). The morphology of astrocytes also changes with age in a brain region specific manner (Cerbai et al., 2012; Rodríguez et al., 2014), which is consistent with the rearrangement of the astrocyte endfeet that may accompany the underlying pia membrane expansion.

It is less clear whether neuroinflammation, BBB leakage, and blockage of fluid flow also contribute to the observed age effects. Although microglia can develop an inflammatory profile with aging (Clarke et al., 2018; DiSabato et al., 2016), accumulation of infiltrated leucocytes in the PVSVs which are necessary for explaining the observed PVSV enlargement (Wuerfel et al., 2008) has not been reported in healthy subjects. Some earlier studies suggested that BBB integrity gradually declines with age as evidenced by

Author Manuscript Author Manuscript Author Manuscript Author Manuscript

perivascular IgG extravasation and tight junction changes in the hippocampus and thalamus (Bake et al., 2009) and increased CSF to plasma albumin ratio in older healthy subjects (Farrall and Wardlaw, 2009). However, no significant age effect was observed in thalamus in our study and a recent contrast MRI study found no significant BBB leakage in WM and subcortical structures except caudate nucleus in old compared to young individuals with no cognitive impairment (Montagne et al., 2015). Lastly, blockage of glymphatic fluid flow seems unlikely to be present in our healthy participants.

4.3. Inter-subject variations and spatial heterogeneity

The count and VF of PVSVs showed large inter-subject variations, with residual COV ranging from 0.17 to 0.74, after regressing out the age and gender effects. VF also showed large spatial heterogeneity (Fig. 5B). On the other hand, the inter-subject and spatial variations were much less for rCNR and apparent diameter (Table 5 and Fig. 5A and C), which can be explained by the sampling bias in calculating mean rCNRs and apparent diameters, which were based only on PVSVs that were large enough to be visualized in the images. The strong VF heterogeneity and large inter-subject variations in VF and count suggest that there might exist large variations in the true PVSV diameter distributions across brain regions and subjects, such that different fractions of PVSVs were large enough to be visualized in MRI in different subjects and brain regions. Genetic heterogeneity among participants might have contributed to the inter-subject variation of PVSV morphology. In a large population-based study of >1500 stroke- and dementia-free older subjects (age 72.8 ± 4.1 yrs), 59% of the variations in global PVSV load rating could be attributed to genetic effects (Duperron et al., 2018). We note that the observed range for total PVSV count (451–2314) is comparable to those reported in (Feldman et al., 2018), where the count ranged from ~500 to ~4000 and was below 2500 in the majority (80%) of subjects.

The heterogeneities in PVSV diameter and VF may have important implications in evaluating the clinical significance of PVSVs. Earlier studies found that, compared to healthy controls, PVSVs in BG were more common in patients with vascular dementia (Banerjee et al., 2017; Hansen et al., 2015; Patankar et al., 2005), blood brain barrier impairment (Li et al., 2019), WMH, lacunar infarct, and deep and infratentorial CMB (Charidimou et al., 2013; Doubal et al., 2010; Duperron et al., 2018; Martinez-Ramirez et al., 2013; Rouhl et al., 2008; Yakushiji et al., 2014; Yamada et al., 2019), while PVSV in centrum semiovale showed smaller or no difference between the patient and control groups. On the other hand, the enlarged PVSVs in centrum semiovale were more strongly associated with strictly lobar CMB which suggests the presence of cerebral amyloid angiopathy (Charidimouetal., 2013; Yakushijiet al., 2014). Our study found that the PVSV diameters in healthy subjects are also different between the two regions, which should be considered when identifying pathologically enlarged PVSVs in these two regions. Furthermore, the PVSV distribution is heterogeneous within both BG and WM and a region with high PVSV volume fraction was found in the sub-insular WM. The spatial pattern of VF resembles the pattern of amyloid-beta deposition in patients with Alzheimer’s disease and non- demented older adults who had significant amyloid deposition (Buckner et al., 2005, 2009). In both cases, highest values were located in the parietal and frontal lobes and sub-insular regions,

Author Manuscript Author Manuscript Author Manuscript Author Manuscript

similar to the VF map in Fig. 4, suggesting that brain regions with more visible PVSVs may have increased risk for impaired glymphatic function later in life.

4.4. Effects of B_1 inhomogeneities on PVSV heterogeneity

We note that the B_1 inhomogeneities (both transmitter and receiver coils) may have partly contributed to the observed heterogeneities in apparent diameter, VF and rCNR. However, it is unlikely to be the sole contribution. In the three non-WM structures, the midbrain had slightly higher rCNR but much lower VF than BG, suggesting that the VF difference was not due to B_1 inhomogeneity induced contrast to noise ratio differences. Within the WM ROIs, ROI_{low} and ROI_{high} had similar image intensities despite higher B_{1t} in ROI_{low}, which could be explained by the higher receiver coil sensitivity in ROIhigh which compensated for the its lower B_{1t}. The similar image intensities suggest that rCNR should also be similar between these two regions for PVSVs of similar sizes. Therefore, the large VF differences between these two regions likely reflect inherent heterogeneity in PVSV morphology within WM. Among the three arterial territories within WM (ACA, MCA, and PCA), the differences in $B_{1,t}$ and image intensities were less than 18% and there was no significant difference in rCNR. However, WM-PCA had 78–79% lower VF than WM- MCA and WM-ACA, which is unlikely to be explained solely by the much smaller B_1 differences.

4.5. Effects of carbogen breathing

Carbogen breathing could have several effects on the observed PVSV signal. First, as demonstrated in our simulation, it increased signal intensity of PVSVs associated with penetrating venules because T_2 in venules became longer under carbogen breathing. In addition, it led to shorter T1 in PAs and PVSs, which resulted in higher signal intensity in both compartments because with the relatively short TR (TR = 3 s) in our imaging protocol, the longitudinal magnetization recovered more before the next TR during carbogen breathing. Second, the hypercapnic effect of carbogen would induce PA dilation (Brian, 1998) which would expel some of the fluid from the PVSs and in turn would reduce PVSV signal, assuming no change in PVS outer diameters, because PVS fluid has higher signal intensity than arterial blood (Table 1). The observed rCNR increases in thalamus, BG, and WM suggest that the first effect was dominant. Increased rCNRs would allow some of the PVSV voxels with strong partial volume effects to be visualized only under carbogen, but not air breathing condition, consistent with the significantly increased VF under carbogen breathing in BG and WM. Furthermore, we observed ~0.01 mm increase in apparent diameter for PVSVs in WM. Because of the much larger voxel size (0.4 mm) of the T_2w images relative to this change, this apparent increase may not represent true PVSV dilation but can instead be explained by the increased number of visualized PVSV voxels under carbogen breathing, since the apparent diameter was calculated based on the number of PVSV voxels associated with VoPs using Eq. (1). According to Eq. (1), 1.6% increase in apparent diameter (Table 6) corresponds to 3.2% increase in $N_{nearest}$. Out results suggest that potential biochemical changes in the PVS fluid and blood that affect their magnetic resonance properties should be considered while studying PVSV morphology in the future. Whether or not the age-related changes in the biochemical compositions of PVS fluid and blood contributed to the observed age dependence of PVSV morphology remains to be determined.

Author Manuscript Author Manuscript Author Manuscript Author Manuscript

4.6. Limitations

The current study has the following limitations. First, the maximum age of our participants was only 55, which is younger than the typical ages (≥65) at which neurodegenerative diseases occur, such as small vessel disease (Bokura et al., 2006; Kuller et al., 2004; Longstreth et al., 1996; Vermeer et al., 2003) and Alzheimer's disease (Alzheimer's Association, 2016). Therefore, our data cannot serve as a direct reference for ascertaining abnormal PVSV dilations in older patients. Second, despite the high spatial resolution adopted in the study, partial volume effects were still present in the PVSV voxels. As a result, the blood and PVS contributions cannot be separated. Further, the apparent diameters and VFs might be overestimated as PVSVs occupied only part of the PVSV voxels and the effects were sensitive to biochemical compositions of blood and PVS fluid. Third, carbogen flow rate was fixed and end-tidal CO_2 levels were not measured, which could result in variations in arterial CO_2 levels among the subjects during carbogen breathing. Fourth, there existed strong B_1 inhomogeneities which might have contributed to the observed PVS heterogeneities. Fifth, there may exist some errors in delineating different PVSV by clustering. A single PVSV might be separated into two if some voxels in the middle were not segmented due to low contrast. However, since the spatial contextual information could also be learned during network training, the fraction of such missing PVSV voxels was likely low. In addition, two PVSVs might have been clustered as one PVSV if two voxels with one from each PVSV were nearest neighbors. The fraction of such PVSVs is also expected to be low except in brain regions with high VFs, such as the BG and sub-insular region. Further studies are needed to quantify the errors in the clustering results.

5. Conclusions

In conclusion, we found increased PVSV VF, count, and rCNR with age in healthy adults. Their morphological features are heterogeneous and show large inter-subject variations. Increased PVSV apparent diameter, VF, and rCNR were observed during carbogen breathing compared to air breathing, suggesting the sensitivity of PVSV morphology to physiological conditions.

Acknowledgements

This study was supported by the United States NIH grant 5R21NS095027-02. We thank Sheng-Che Hung, M.D. and the anonymous reviewers for their invaluable comments and suggestions.

References

Adachi M, Hosoya T, Haku T, Yamaguchi K, 1998 Dilated Virchow-Robin spaces: MRI pathological study. Neuroradiology 40, 27–31. [PubMed: 9493184]

Alzheimer's Association, 2016 2016 Alzheimer's disease facts and figures. Alzheimers Dement 12, 459–509. [PubMed: 27570871]

An H, Sen S, Chen Y, Powers WJ, Lin W, 2012 Noninvasive measurements of cerebral blood flow, oxygen extraction fraction, and oxygen metabolic index in human with inhalation of air and carbogen using magnetic resonance imaging. Transl. Stroke Res 3, 246–254. [PubMed: 24323780]

Anzai Y, Ishikawa M, Shaw DWW, Artru A, Yarnykh V, Maravilla KR, 2004 Paramagnetic effect of supplemental oxygen on CSF hyperintensity on fluid- attenuated inversion recovery MR images. Am. J. Neuroradiol 25, 274. [PubMed: 14970030]

Author Manuscript Author Manuscript Author Manuscript Author Manuscript

Aribisala BS, Wiseman S, Morris Z, Valdes-Hernandez MC, Royle NA, Maniega SM, Gow AJ, Corley J, Bastin ME, Starr J, Deary IJ, Wardlaw JM, 2014 Circulating inflammatory markers are associated with magnetic resonance imaging-visible perivascular spaces but not directly with white matter hyperintensities. Stroke 45, 605–607. [PubMed: 24399375]

Avants BB, Tustison NJ, Song G, Cook PA, Klein A, Gee JC, 2011 A reproducible evaluation of ANTs similarity metric performance in brain image registration. Neuroimage 54, 2033–2044. [PubMed: 20851191]

Awad IA, Johnson PC, Spetzler RF, Hodak JA, 1986 Incidental subcortical lesions identified on magnetic resonance imaging in the elderly. II. Postmortem pathological correlations. Stroke 17, 1090–1097. [PubMed: 3810706]

Bake S, Friedman JA, Sohrabji F, 2009 Reproductive age-related changes in the blood brain barrier: expression of IgG and tight junction proteins. Microvasc. Res 78, 413–424. [PubMed: 19591848]

Banerjee G, Kim HJ, Fox Z, Jager HR, Wilson D, Charidimou A, Na HK, Na DL, Seo SW, Werring DJ, 2017 MRI-visible perivascular space location is associated with Alzheimer's disease independently of amyloid burden. Brain 140, 1107–1116. [PubMed: 28335021]

Benhaïem-Sigaux N, Gray F, Gherardi R, Roucayrol AM, Poirier J, 1987 Expanding cerebellar lacunes due to dilatation of the perivascular space associated with Binswanger's subcortical arteriosclerotic encephalopathy. Stroke 18, 1087–1092. [PubMed: 3686582]

Bishop CA, Newbould RD, Lee JS, Honeyfield L, Quest R, Colasanti A, Ali R, Mattoscio M, Cortese A, Nicholas R, Matthews PM, Muraro PA, Waldman AD, 2017 Analysis of ageing-associated grey matter volume in patients with multiple sclerosis shows excess atrophy in subcortical regions. Neuroimage Clin. 13, 9–15. [PubMed: 27896065]

Bloembergen N, Morgan LO, 1961 Proton relaxation times in paramagnetic solutions. Effects of electron spin relaxation. J. Chem. Phys 34, 842–850.

Boespflug EL, Schwartz DL, Lahna D, Pollock J, Iliff JJ, Kaye JA, Rooney W, Silbert LC, 2018a MR imaging-based multimodal autoidentification of perivascular spaces (mMAPS): automated morphologic segmentation of enlarged perivascular spaces at clinical field strength. Radiology 286, 632–642. [PubMed: 28853674]

Boespflug EL, Simon MJ, Leonard E, Grafe M, Woltjer R, Silbert LC, Kaye JA, Iliff JJ, 2018b Targeted assessment of enlargement of the perivascular space in alzheimer's disease and vascular dementia subtypes implicates astroglial involvement specific to alzheimer's disease. J. Alzheimers Dis 66, 1587–1597. [PubMed: 30475760]

Bokura H, Kobayashi S, Yamaguchi S, Iijima K, Nagai A, Toyoda G, Oguro H, Takahashi K, 2006 Silent brain infarction and subcortical white matter lesions increase the risk of stroke and mortality: a prospective cohort study. J. Stroke Cerebrovasc. Dis 15, 57–63. [PubMed: 17904049]

Bouvy WH, Zwanenburg JJM, Reinink R, Wisse LEM, Luijten PR, Kappelle LJ, Geerlings MI, Biessels GJ, Utrecht Vascular Cognitive Impairment Study, g, 2016 Perivascular spaces on 7 Tesla brain MRI are related to markers of small vessel disease but not to age or cardiovascular risk factors. J. Cerebr. Blood Flow Metabol 36, 1708–1717.

Brian JE Jr., 1998 Carbon dioxide and the cerebral circulation. Anesthesiology 88, 1365–1386. [PubMed: 9605698]

Brown WR, Moody DM, Challa VR, Thore CR, Anstrom JA, 2002 Venous collagenosis and arteriolar tortuosity in leukoaraiosis. J. Neurol. Sci 203–204, 159–163.

Buckner RL, Sepulcre J, Talukdar T, Krienen FM, Liu H, Hedden T, Andrews-Hanna JR, Sperling RA, Johnson KA, 2009 Cortical hubs revealed by intrinsic functional connectivity: mapping, assessment of stability, and relation to Alzheimer' s disease. J. Neurosci. 29, 1860–1873. [PubMed: 19211893]

Buckner RL, Snyder AZ, Shannon BJ, LaRossa G, Sachs R, Fotenos AF, Sheline YI, Klunk WE, Mathis CA, Morris JC, Mintun MA, 2005 Molecular, structural, and functional characterization of Alzheimer's disease: evidence for a relationship between default activity, amyloid, and memory. J. Neurosci 25, 7709–7717. [PubMed: 16120771]

Busse RF, Hariharan H, Vu A, Brittain JH, 2006 Fast spin echo sequences with very long echo trains: design of variable refocusing flip angle schedules and generation of clinical T2 contrast. Magn. Reson. Med 55, 1030–1037. [PubMed: 16598719]

Author Manuscript Author Manuscript Author Manuscript Author Manuscript

Cai K, Tain R, Das S, Damen FC, Sui Y, Valyi-Nagy T, Elliott MA, Zhou XJ, 2015 The feasibility of quantitative MRI of perivascular spaces at 7T. J. Neurosci. Methods 256, 151–156. [PubMed: 26358620]

Cerbai F, Lana D, Nosi D, Petkova-Kirova P, Zecchi S, Brothers HM, Wenk GL, Giovannini MG, 2012 The neuron-astrocyte-microglia triad in normal brain ageing and in a model of neuroinflammation in the rat hippocampus. PloS One 7, e45250. [PubMed: 23028880]

Charidimou A, Meegahage R, Fox Z, Peeters A, Vandermeeren Y, Laloux P, Baron JC, Jager HR, Werring DJ, 2013 Enlarged perivascular spaces as a marker of underlying arteriopathy in intracerebral haemorrhage: a multicentre MRI cohort study. J. Neurol. Neurosurg. Psychiatry 84, 624–629. [PubMed: 23412074]

Chen W, Song X, Zhang Y, Alzheimer's Disease Neuroimaging, I, 2011 Assessment of the Virchow-Robin Spaces in Alzheimer disease, mild cognitive impairment, and normal aging, using high-field MR imaging. AJNR Am. J. Neuroradiol 32, 1490–1495. [PubMed: 21757525]

Clarke LE, Liddelow SA, Chakraborty C, Münch AE, Heiman M, Barres BA, 2018 Normal aging induces A1-like astrocyte reactivity. Proc. Natl. Acad. Sci. U. S. A 115, E1896–e1905. [PubMed: 29437957]

Cox RW, 1996 AFNI: software for analysis and visualization of functional magnetic resonance neuroimages. Comput. Biomed. Res 29, 162–173. [PubMed: 8812068]

DeCarli C, Massaro J, Harvey D, Hald J, Tullberg M, Au R, Beiser A, D'Agostino R, Wolf PA, 2005 Measures of brain morphology and infarction in the framingham heart study: establishing what is normal. Neurobiol. Aging 26, 491–510. [PubMed: 15653178]

Derouesné C, Gray F, Escourolle R, Castaigne P, 1987 Expanding cerebral lacunae' in a hypertensive patient with normal pressure hydrocephalus. Neuropathol. Appl. Neurobiol 13, 309–320. [PubMed: 3658108]

Ding J, Sigurethsson S, Jonsson PV, Eiriksdottir G, Charidimou A, Lopez OL, van Buchem MA, Guethnason V, Launer LJ, 2017 Large perivascular spaces visible on magnetic resonance imaging, cerebral small vessel disease progression, and risk of dementia: the age, gene/environment susceptibility-reykjavik study. JAMA Neurol. 74, 1105–1112. [PubMed: 28715552]

DiSabato DJ, Quan N, Godbout JP, 2016 Neuroinflammation: the devil is in the details. J. Neurochem 139 (Suppl. 2), 136–153. [PubMed: 26990767]

Doubal FN, MacLullich AM, Ferguson KJ, Dennis MS, Wardlaw JM, 2010 Enlarged perivascular spaces on MRI are a feature of cerebral small vessel disease. Stroke 41, 450–454. [PubMed: 20056930]

Duperron MG, Tzourio C, Sargurupremraj M, Mazoyer B, Soumare A, Schilling S, Amouyel P, Chauhan G, Zhu YC, Debette S, 2018 Burden of dilated perivascular spaces, an emerging marker of cerebral small vessel disease, is highly heritable. Stroke 49, 282–287. [PubMed: 29311265]

Duperron MG, Tzourio C, Schilling S, Zhu YC, Soumare A, Mazoyer B, Debette S, 2019 High dilated perivascular space burden: a new MRI marker for risk of intracerebral hemorrhage. Neurobiol. Aging 84, 158–165. [PubMed: 31629114]

Farrall AJ, Wardlaw JM, 2009 Blood-brain barrier: ageing and microvascular disease-systematic review and meta-analysis. Neurobiol. Aging 30, 337–352. [PubMed: 17869382]

Feldman RE, Rutland JW, Fields MC, Marcuse LV, Pawha PS, Delman BN, Balchandani P, 2018 Quantification of perivascular spaces at 7T: a potential MRI biomarker for epilepsy. Seizure 54, 11–18. [PubMed: 29172093]

Fjell AM, Westlye LT, Amlien I, Espeseth T, Reinvang I, Raz N, Agartz I, Salat DH, Greve DN, Fischl B, Dale AM, Walhovd KB, 2009 Minute effects of sex on the aging brain: a multisample magnetic resonance imaging study of healthy aging and Alzheimer's disease. J. Neurosci 29, 8774–8783. [PubMed: 19587284]

Fonov V, Evans AC, Botteron K, Almli CR, McKinstry RC, Collins DL, Brain Development Cooperative G, 2011 Unbiased average age-appropriate atlases for pediatric studies. Neuroimage 54, 313–327. [PubMed: 20656036]

Gallichan D, Marques JP, Gruetter R, 2016 Retrospective correction of involuntary microscopic head movement using highly accelerated fat image navigators (3D FatNavs) at 7T. Magn. Reson. Med 75, 1030–1039. [PubMed: 25872755]

Author Manuscript Author Manuscript Author Manuscript Author Manuscript

Good CD, Johnsrude IS, Ashburner J, Henson RNA, Friston KJ, Frackowiak RSJ, 2001 A voxel-based morphometric study of ageing in 465 normal adult human brains. Neuroimage 14, 21–36. [PubMed: 11525331]

Goodro M, Sameti M, Patenaude B, Fein G, 2012 Age effect on subcortical structures in healthy adults. Psychiatr. Res. Neuroimaging 203, 38–45.

Grgac K, van Zijl PC, Qin Q, 2013 Hematocrit and oxygenation dependence of blood (1)H(2)O T(1) at 7 Tesla. Magn. Reson. Med 70, 1153–1159. [PubMed: 23169066]

Grieve SM, Clark CR, Williams LM, Peduto AJ, Gordon E, 2005 Preservation of limbic and paralimbic structures in aging. Hum. Brain Mapp 25, 391–401. [PubMed: 15852381]

Gutierrez J, Elkind MSV, Dong C, Di Tullio M, Rundek T, Sacco RL, Wright CB, 2017 Brain perivascular spaces as biomarkers of vascular risk: results from the northern manhattan study. AJNR Am. J. Neuroradiol 38, 862–867. [PubMed: 28341719]

Hansen TP, Cain J, Thomas O, Jackson A, 2015 Dilated perivascular spaces in the Basal Ganglia are a biomarker of small-vessel disease in a very elderly population with dementia. AJNR Am. J. Neuroradiol 36, 893–898. [PubMed: 25698626]

Heier LA, Bauer CJ, Schwartz L, Zimmerman RD, Morgello S, Deck MD, 1989 Large Virchow-Robin spaces: MR-clinical correlation. AJNR Am. J. Neuroradiol 10, 929–936. [PubMed: 2505536]

Hennig J, 1988 Multiecho imaging sequences with low refocusing flip angles. J. Magn. Reson 78, 397–407.

Homeyer P, Cornu P, Lacomblez L, Chiras J, Derouesné C, 1996 A special form of cerebral lacunae: expanding lacunae. J. Neurol. Neurosurg. Psychiatry 61, 200–202. [PubMed: 8708692]

Hughes W, 1965 Hypothesis. Lancet 286, 19–21.

Iliff JJ, Wang M, Liao Y, Plogg BA, Peng W, Gundersen GA, Benveniste H, Vates GE, Deane R, Goldman SA, Nagelhus EA, Nedergaard M, 2012 A paravascular pathway facilitates CSF flow through the brain parenchyma and the clearance of interstitial solutes, including amyloid beta. Sci. Transl. Med 4, 147ra111.

Inano S, Takao H, Hayashi N, Yoshioka N, Mori H, Kunimatsu A, Abe O, Ohtomo K, 2013 Effects of age and gender on neuroanatomical volumes. J. Magn. Reson. Imag 37, 1072–1076.

Inglese M, Bomsztyk E, Gonen O, Mannon LJ, Grossman RI, Rusinek H, 2005 Dilated perivascular spaces: hallmarks of mild traumatic brain injury. AJNR Am. J. Neuroradiol 26, 719–724. [PubMed: 15814911]

Kilsdonk ID, Steenwijk MD, Pouwels PJ, Zwanenburg JJ, Visser F, Luijten PR, Geurts J, Barkhof F, Wattjes MP, 2015 Perivascular spaces in MS patients at 7 Tesla MRI: a marker of neurodegeneration? Mult. Scler 21, 155–162. [PubMed: 25013150]

Kim DE, Park JH, Schellingerhout D, Ryu WS, Lee SK, Jang MU, Jeong SW, Na JY, Park JE, Lee EJ, Cho KH, Kim JT, Kim BJ, Han MK, Lee J, Cha JK, Kim DH, Lee SJ, Ko Y, Lee BC, Yu KH, Oh MS, Hong KS, Cho YJ, Park JM, Kang K, Park TH, Lee KB, Park KJ, Choi HK, Lee J, Bae HJ, 2019 Mapping the supratentorial cerebral arterial territories using 1160 large artery infarcts. JAMA Neurol. 76, 72–80. [PubMed: 30264158]

Koo HW, Oh M, Kang HK, Park YK, Lee BJ, Han SR, Yoon SW, Choi CY, Sohn MJ, Lee CH, 2019 High-degree centrum semiovale-perivascular spaces are associated with development of subdural fluid in mild traumatic brain injury. PloS One 14, e0221788. [PubMed: 31483820]

Kruggel F, 2006 MRI-based volumetry of head compartments: normative values of healthy adults. Neuroimage 30, 1–11. [PubMed: 16289929]

Kuller LH, Longstreth WT Jr., Arnold AM, Bernick C, Bryan RN, Beauchamp NJ Jr., Cardiovascular Health Study Collaborative Research, G., 2004 White matter hyperintensity on cranial magnetic resonance imaging: a predictor of stroke. Stroke 35, 1821–1825. [PubMed: 15178824]

Lau KK, Li L, Lovelock CE, Zamboni G, Chan TT, Chiang MF, Lo KT, Kuker W, Mak HK, Rothwell PM, 2017 Clinical correlates, ethnic differences, and prognostic implications of perivascular spaces in transient ischemic attack and ischemic stroke. Stroke 48, 1470–1477. [PubMed: 28495831]

Li W, van Zijl PCM, 2020 Quantitative theory for the transverse relaxation time of blood water. NMR Biomed. 33, e4207. [PubMed: 32022362]

Author Manuscript Author Manuscript Author Manuscript Author Manuscript

Li Y, Li M, Yang L, Qin W, Yang S, Yuan J, Jiang T, Hu W, 2019 The relationship between blood-brain barrier permeability and enlarged perivascular spaces: a cross-sectional study. Clin. Interv. Aging 14, 871–878. [PubMed: 31190773]

Lian C, Zhang J, Liu M, Zong X, Hung SC, Lin W, Shen D, 2018 Multi-channel multi-scale fully convolutional network for 3D perivascular spaces segmentation in 7T MR images. Med. Image Anal 46, 106–117. [PubMed: 29518675]

Liu P, De Vis JB, Lu H, 2019 Cerebrovascular reactivity (CVR) MRI with CO2 challenge: a technical review. Neuroimage 187, 104–115. [PubMed: 29574034]

Longstreth WT Jr., Manolio TA, Arnold A, Burke GL, Bryan N, Jungreis CA, Enright PL, O'Leary D, Fried L, 1996 Clinical correlates of white matter findings on cranial magnetic resonance imaging of 3301 elderly people. The Cardiovascular Health Study. Stroke 27, 1274–1282. [PubMed: 8711786]

Ma Y, Berman AJ, Pike GB, 2016 The effect of dissolved oxygen on the relaxation rates of blood plasma: implications for hyperoxia calibrated BOLD. Magn. Reson. Med 76, 1905–1911. [PubMed: 26628286]

Martinez-Ramirez S, Pontes-Neto OM, Dumas AP, Auriel E, Halpin A, Quimby M, Gurol ME, Greenberg SM, Viswanathan A, 2013 Topography of dilated perivascular spaces in subjects from a memory clinic cohort. Neurology 80, 1551–1556. [PubMed: 23553482]

Mehemed TM, Fushimi Y, Okada T, Yamamoto A, Kanagaki M, Kido A, Fujimoto K, Sakashita N, Togashi K, 2014 Dynamic oxygen-enhanced MRI of cerebrospinal fluid. PloS One 9, e100723. [PubMed: 24956198]

Montagne A, Barnes SR, Sweeney MD, Halliday MR, Sagare AP, Zhao Z, Toga AW, Jacobs RE, Liu CY, Amezcua L, Harrington MG, Chui HC, Law M, Zlokovic BV, 2015 Blood-brain barrier breakdown in the aging human hippocampus. Neuron 85, 296–302. [PubMed: 25611508]

Mutsaerts HJ, van Dalen JW, Heijtel DF, Groot PF, Majoie CB, Petersen ET, Richard E, Nederveen AJ, 2015 Cerebral perfusion measurements in elderly with hypertension using arterial spin labeling. PloS One 10, e0133717. [PubMed: 26241897]

Narvacan K, Treit S, Camicioli R, Martin W, Beaulieu C, 2017 Evolution of deep gray matter volume across the human lifespan. Hum. Brain Mapp 38, 3771–3790. [PubMed: 28548250]

Oishi K, Zilles K, Amunts K, Faria A, Jiang H, Li X, Akhter K, Hua K, Woods R, Toga AW, Pike GB, Rosa-Neto P, Evans A, Zhang J, Huang H, Miller MI, van Zijl PC, Mazziotta J, Mori S, 2008 Human brain white matter atlas: identification and assignment of common anatomical structures in superficial white matter. Neuroimage 43, 447–457. [PubMed: 18692144]

Opel RA, Christy A, Boespflug EL, Weymann KB, Case B, Pollock JM, Silbert LC, Lim MM, 2019 Effects of traumatic brain injury on sleep and enlarged perivascular spaces. J. Cerebr. Blood Flow Metabol 39, 2258–2267.

Park YS, Chung MS, Choi BS, 2019a MRI assessment of cerebral small vessel disease in patients with spontaneous intracerebral hemorrhage. Yonsei Med. J 60, 774–781. [PubMed: 31347333]

Park YW, Shin NY, Chung SJ, Kim J, Lim SM, Lee PH, Lee SK, Ahn KJ, 2019b Magnetic resonance imaging-visible perivascular spaces in basal ganglia predict cognitive decline in Parkinson's disease. Mov. Disord 34, 1672–1679. [PubMed: 31322758]

Patankar TF, Mitra D, Varma A, Snowden J, Neary D, Jackson A, 2005 Dilatation of the Virchow-Robin space is a sensitive indicator of cerebral microvascular disease: study in elderly patients with dementia. AJNR Am. J. Neuroradiol 26, 1512–1520. [PubMed: 15956523]

Pesce C, Carli F, 1988 Allometry of the perivascular spaces of the putamen in aging. Acta Neuropathol. 76, 292–294. [PubMed: 3213433]

Poirier J, Barbizet J, Gaston A, Meyrignac C, 1983 [Thalamic dementia. Expansive lacunae of the thalamo-paramedian mesencephalic area. Hydrocephalus caused by stenosis of the aqueduct of Sylvius]. Rev. Neurol. (Paris) 139, 349–358. [PubMed: 6137053]

Pollock H, Hutchings M, Weller RO, Zhang ET, 1997 Perivascular spaces in the basal ganglia of the human brain: their relationship to lacunes. J. Anat 191 (Pt 3), 337–346. [PubMed: 9418990]

Potvin O, Mouiha A, Dieumegarde L, Duchesne S, 2016 Normative data for subcortical regional volumes over the lifetime of the adult human brain. Neuroimage 137, 9–20. [PubMed: 27165761]

Author Manuscript Author Manuscript Author Manuscript Author Manuscript

Rasmussen MK, Mestre H, Nedergaard M, 2018 The glymphatic pathway in neurological disorders. Lancet Neurol. 17, 1016–1024. [PubMed: 30353860]

Rodríguez JJ, Yeh C-Y, Terzieva S, Olabarria M, Kulijewicz-Nawrot M, Verkhratsky A, 2014 Complex and region-specific changes in astroglial markers in the aging brain. Neurobiol. Aging 35, 15–23. [PubMed: 23969179]

Rouhl RP, van Oostenbrugge RJ, Knottnerus IL, Staals JE, Lodder J, 2008 Virchow-Robin spaces relate to cerebral small vessel disease severity. J. Neurol 255, 692–696. [PubMed: 18286319]

Savalia NK, Agres PF, Chan MY, Feczko EJ, Kennedy KM, Wig GS, 2017 Motion-related artifacts in structural brain images revealed with independent estimates of in-scanner head motion. Hum. Brain Mapp 38, 472–492. [PubMed: 27634551]

Severinghaus JW, 1979 Simple, accurate equations for human blood O2 dissociation computations. J. Appl. Physiol. Respir. Environ. Exerc. Physiol 46, 599–602. [PubMed: 35496]

Smith CD, Chebrolu H, Wekstein DR, Schmitt FA, Markesbery WR, 2007 Age and gender effects on human brain anatomy: a voxel-based morphometric study in healthy elderly. Neurobiol. Aging 28, 1075–1087. [PubMed: 16774798]

Smith SM, 2002 Fast robust automated brain extraction. Hum. Brain Mapp 17, 143–155. [PubMed: 12391568]

Song TJ, Park JH, Choi KH, Chang Y, Moon J, Kim JH, Choi Y, Kim YJ, Lee HW, 2017 Moderate-to-severe obstructive sleep apnea is associated with cerebral small vessel disease. Sleep Med. 30, 36–42. [PubMed: 28215260]

Spangler KM, Challa VR, Moody DM, Bell MA, 1994 Arteriolar tortuosity of the white matter in aging and hypertension. A microradiographic study. J. Neuropathol. Exp. Neurol 53, 22–26. [PubMed: 8301316]

Thore CR, Anstrom JA, Moody DM, Challa VR, Marion MC, Brown WR, 2007 Morphometric analysis of arteriolar tortuosity in human cerebral white matter of preterm, young, and aged subjects. J. Neuropathol. Exp. Neurol 66, 337–345. [PubMed: 17483690]

Tripathi A, Bydder GM, Hughes JM, Pennock JM, Goatcher A, Orr JS, Steiner RE, Greenspan RH, 1984 Effect of oxygen tension on NMR spin-lattice relaxation rate of blood in vivo. Invest. Radiol 19, 174–178. [PubMed: 6469521]

Tullo S, Patel R, Devenyi GA, Salaciak A, Bedford SA, Farzin S, Wlodarski N, Tardif CL, Breitner JCS, Chakravarty MM, 2019 MR-based age-related effects on the striatum, globus pallidus, and thalamus in healthy individuals across the adult lifespan. Hum. Brain Mapp 40, 5269–5288. [PubMed: 31452289]

Vermeer SE, Hollander M, van Dijk EJ, Hofman A, Koudstaal PJ, Breteler MM, Rotterdam Scan S, 2003 Silent brain infarcts and white matter lesions increase stroke risk in the general population: the Rotterdam Scan Study. Stroke 34, 1126–1129. [PubMed: 12690219]

Wuerfel J, Haertle M, Waiczies H, Tysiak E, Bechmann I, Wernecke KD, Zipp F, Paul F, 2008 Perivascular spaces-MRI marker of inflammatory activity in the brain? Brain 131, 2332–2340. [PubMed: 18676439]

Xu X, Wang B, Ren C, Hu J, Greenberg DA, Chen T, Xie L, Jin K, 2017 Age-related impairment of vascular structure and functions. Aging Dis. 8, 590–610. [PubMed: 28966804]

Yakushiji Y, Charidimou A, Hara M, Noguchi T, Nishihara M, Eriguchi M, Nanri Y, Nishiyama M, Werring DJ, Hara H, 2014 Topography and associations of perivascular spaces in healthy adults: the Kashima scan study. Neurology 83, 2116–2123. [PubMed: 25361776]

Yamada S, Ishikawa M, Yamamoto K, Yamaguchi M, Oshima M, 2019 Location-specific characteristics of perivascular spaces as the brain's interstitial fluid drainage system. J. Neurol. Sci 398, 9–15. [PubMed: 30665070]

Zaharchuk G, Martin AJ, Rosenthal G, Manley GT, Dillon WP, 2005 Measurement of cerebrospinal fluid oxygen partial pressure in humans using MRI. Magn. Reson. Med. 54, 113–121. [PubMed: 15968660]

Zhang ET, Inman CB, Weller RO, 1990 Interrelationships of the pia mater and the perivascular (Virchow-Robin) spaces in the human cerebrum. J. Anat 170, 111–123. [PubMed: 2254158]

Author Manuscript Author Manuscript Author Manuscript Author Manuscript

Zhu YC, Tzourio C, Soumare A, Mazoyer B, Dufouil C, Chabriat H, 2010 Severity of dilated Virchow-Robin spaces is associated with age, blood pressure, and MRI markers of small vessel disease: a population-based study. Stroke 41, 2483–2490. [PubMed: 20864661]

Zong X, Park SH, Shen D, Lin W, 2016 Visualization of perivascular spaces in the human brain at 7T: sequence optimization and morphology characterization. Neuroimage 125, 895–902. [PubMed: 26520772]

Author Manuscript Author Manuscript Author Manuscript Author Manuscript

Fig. 1.

The boundaries of the arterial territories overlaid on a T_1-weighted image in the MNI atlas space. Abbreviations: ACA: anterior cerebral artery; MCA: middle cerebral artery; PCA: posterior cerebral artery; WS: watershed region.

Author Manuscript Author Manuscript Author Manuscript Author Manuscript

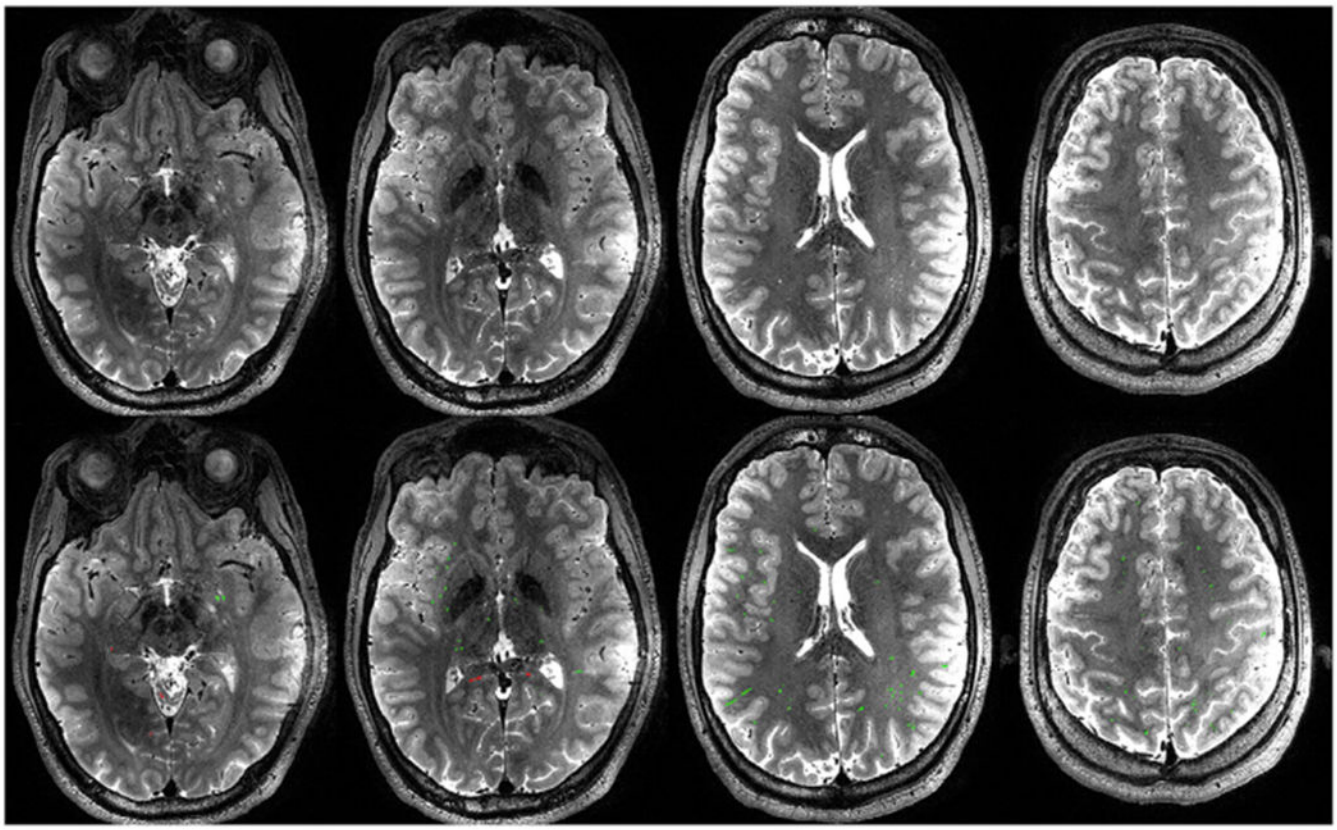

Fig. 2.

Top row: representative T_2W imaging slices in a single subject. Bottom row: PVSV masks generated by the segmentation algorithm overlaid on the same slices, as shown in red and green colors. The red color represents false PVSV voxels that were removed by manual editing.

Author Manuscript Author Manuscript Author Manuscript Author Manuscript

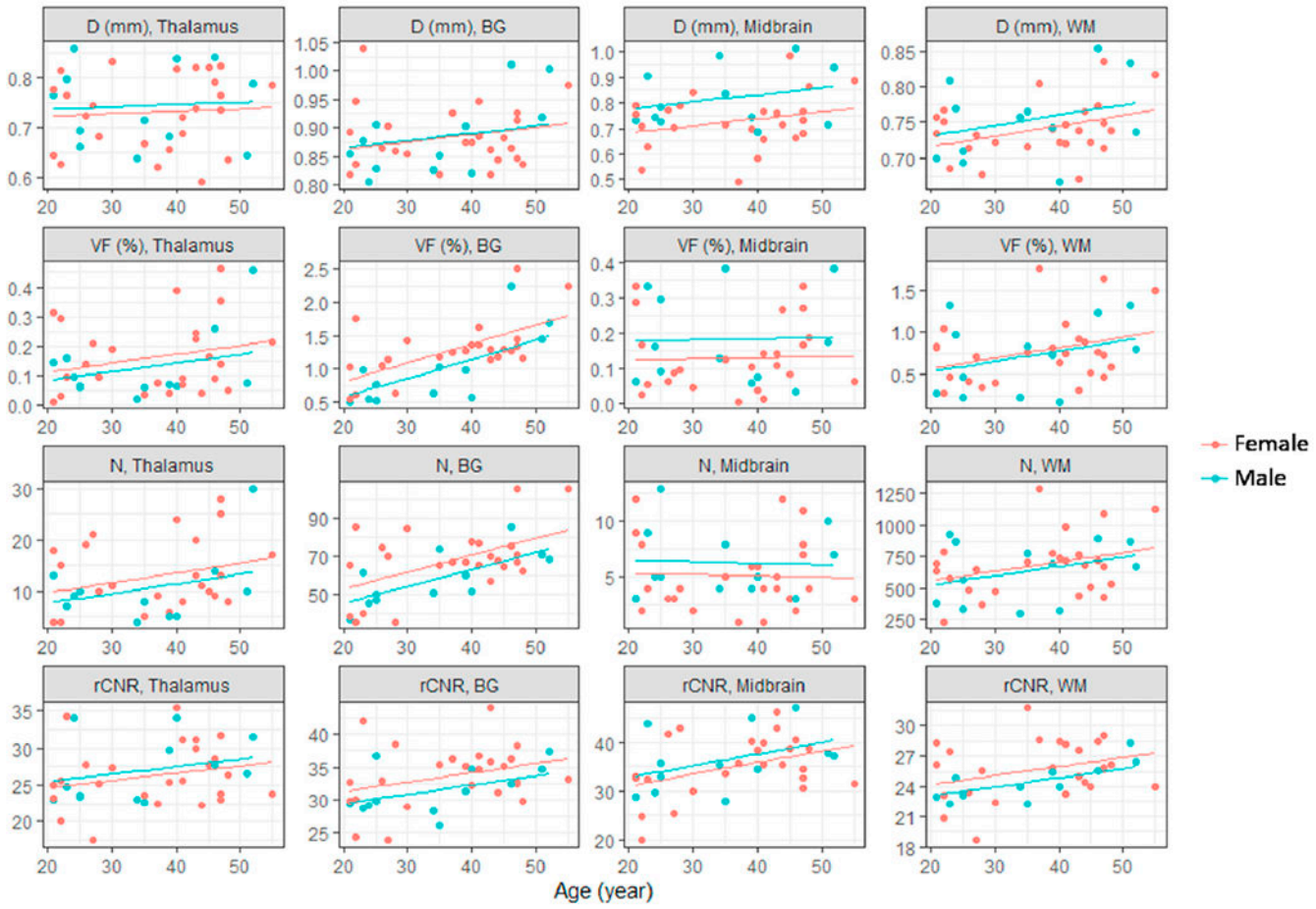

Fig. 3.

Scatter plots of the mean apparent diameter (first row), VF (second row), count (N) (third row), and rCNR (fourth row) of PVSVs versus age and gender in thalamus (first column), BG (second column), midbrain (third column), and WM (fourth column). The lines are best fits from linear regression analyses using age and gender as independent variables.

Author Manuscript Author Manuscript Author Manuscript Author Manuscript

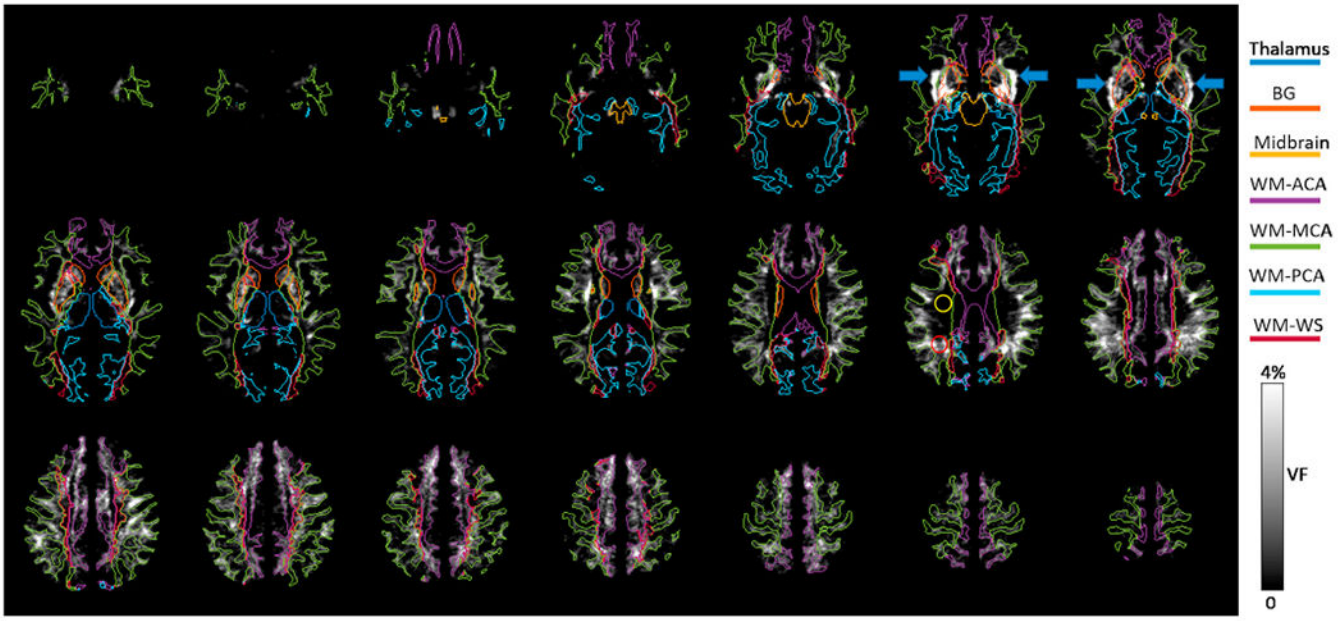

Fig. 4.

The group-averaged PVSV VF map in the MNI atlas space. The boundaries of 7 ROIs are also shown. The yellow and red circles are ROIs covering WM regions with low and high VFs, respectively. The blue arrows point to regions with high VF in the sub-insular WM.

Author Manuscript Author Manuscript Author Manuscript Author Manuscript

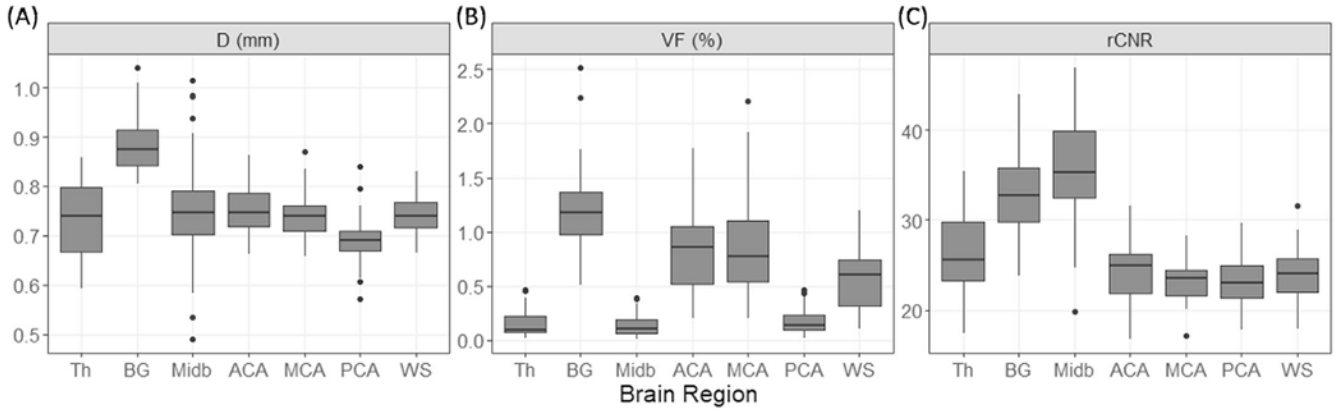

Fig. 5.

Box plots of (A) mean apparent diameter, (B) VF, and (C) rCNR of PVSVs, in 7 ROIs. Abbreviations: Th: thalamus; BG: basal ganglia; Midb: midbrain; ACA: WM-ACA; MCA: WM-MCA; PCA: WM-PCA; WS: WM-WS.

Author Manuscript Author Manuscript Author Manuscript Author Manuscript

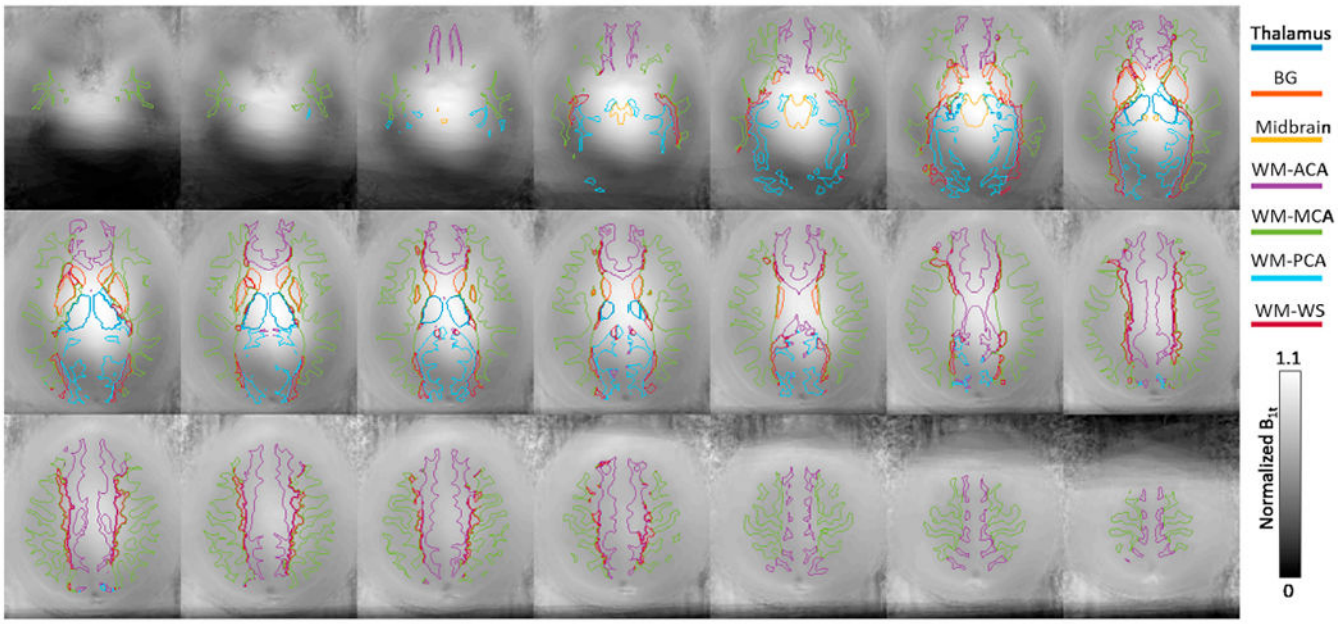

Fig. 6.

Group-averaged transmitter B_1 map in the MNI atlas space. The boundaries of 7 ROIs defined in the study are also shown. The slice positions match those shown in Fig. 4.

Author Manuscript Author Manuscript Author Manuscript Author Manuscript

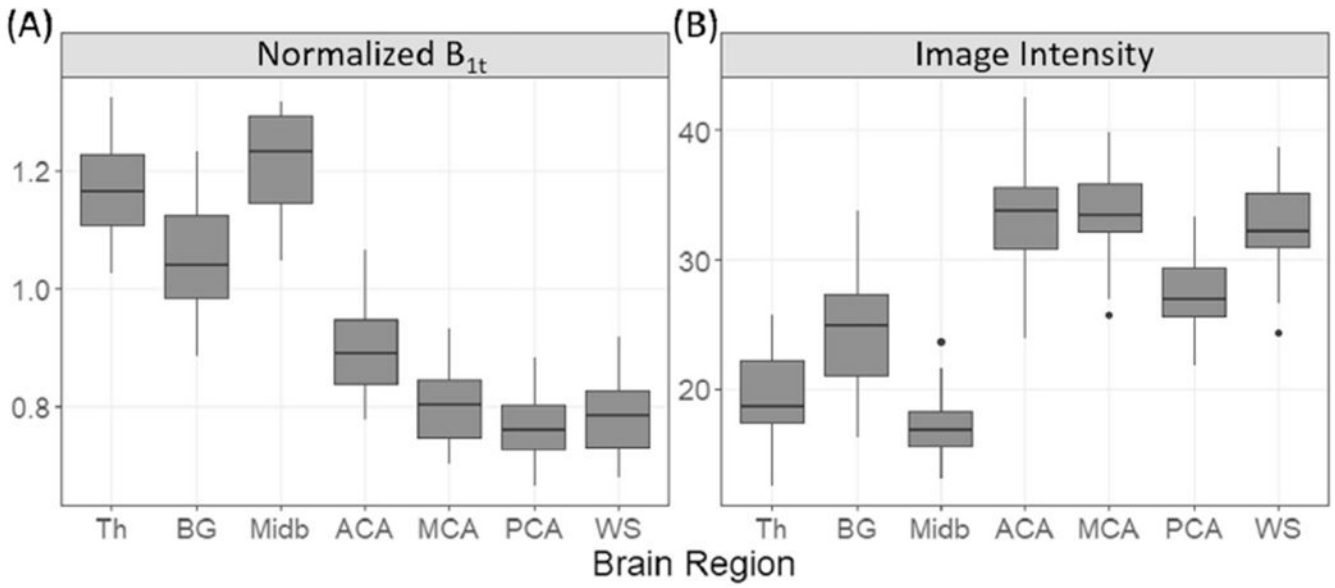

Fig. 7.

Box plots of mean (A) normalized B_{1t} and (B) T_2w image intensity during air breathing in 7 ROIs. Abbreviations: Th: thalamus; BG: basal ganglia; Midb: midbrain; ACA: WM-ACA; MCA: WM-MCA; PCA: WM-PCA; WS: WM-WS.

Author Manuscript Author Manuscript Author Manuscript Author Manuscript

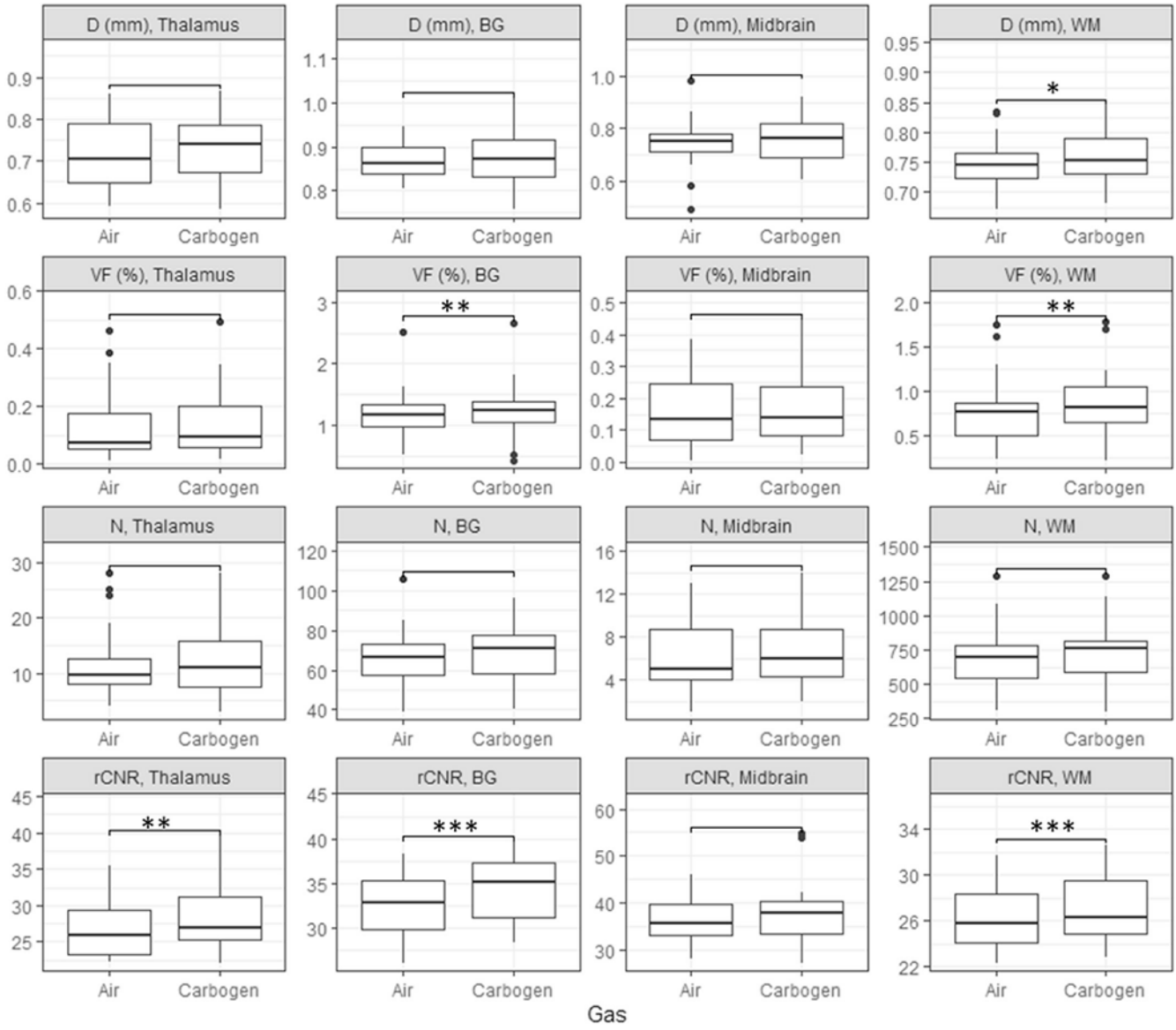

Fig. 8.

Box plots of the mean apparent diameter (first row), VF (second row), count (third row), and rCNR (fourth row) of PVSVs under air and carbogen breathing conditions in thalamus (first column), BG (second column), midbrain (third column), and WM (fourth column). *: $p \leq 0.05$, **: $p \leq 0.005$; ***: $p \leq 0.0005$ from the Wilcoxon's signed rank test after FDR correction .

Author Manuscript Author Manuscript Author Manuscript Author Manuscript

Table 1

Columns 3–6: Model parameters assumed in the simulation. Column 7: the signal intensity at k-space center. Column 8: the relative difference of signal intensities between carbogen and air.

		Y	pO_2 (mmHg)	T1 (ms)	T2 (ms)	Intensity	% intensity change
Venule	Air	0.65	33.9	2057	26.8	0.022	88.2%
	Carbogen	0.75	40.2	2094	40.3	0.042	
Arteriole	Air	0.984	114	2149	82.7	0.0909	1.7%
	Carbogen	0.999	312	2045	82.3	0.0924	
PVS	Air	NA	NA	3500	600	0.216	2.5%
	Carbogen	NA	62	3359	596	0.222	

Neuroimage. Author manuscript; available in PMC 2020 September 11.

Author Manuscript

Author Manuscript

Author Manuscript

Author Manuscript

Table 2

Second column: numbers of subjects who participated in the air and carbogen breathing scans, with and without fat navigator images. The numbers of female subjects and the age ranges of all subjects are given in the parentheses. Third column: numbers of subjects who did not show severe motion artifacts or WMH. Fourth column: numbers of subjects who had both air and carbogen scans and did not show severe motion artifacts or WMH.

	Total	**No motion/WMH**	**No motion/WMH, both air and carb.**
Air	46 (34; age 21–55)	37 (25; age 21–55)	22 (15; age 21–51)
Carbogen	37 (27; age 21–55)	23 (16; age 21–51)	
Air With FatNav	40 (29; age 21–55)	31 (20; age 21–55)	19 (12; age 21–51)
Carbogen with FatNav	33 (23; age 21–55)	20 (13; age 21–51)	

Author Manuscript

Author Manuscript

Author Manuscript

Author Manuscript

Table 3

The means and standard deviations of the motion parameters MT and MR for the female and male participants under the air and carbogen breathing conditions. The numbers of subjects are shown in the parentheses. The p values were obtained from Wilcoxon's rank sum tests comparing values between air and carbogen (A vs C) breathing conditions or between female and male (F vs M) subjects.

	M_T (mm)			M_R (deg)		
	Female	**Male**	**p (F vs M)**	**Female**	**Male**	**P (F vs M)**
Air	0.39 ± 0.11 (20)	0.76 ± 0.45 (11)	0.0006	0.34 ± 0.16 (20)	0.50 ± 0.16 (11)	0.007
Carb.	0.51 ± 0.18 (13)	0.44 ± 0.16 (7)	0.43	0.43 ± 0.14 (13)	0.50 ± 0.24 (7)	0.63
p (A vs C)	0.14	0.044		0.11	0.72	

Author Manuscript

Author Manuscript

Author Manuscript

Author Manuscript

Table 4

The intercepts and coefficients for age (C_{age}) and gender (c_{gender}) obtained from the linear regression analyses of the PVSV mean apparent diameter, VF, count, and rCNR in the thalamus, BG, midbrain, and WM ROIs. Values in the parentheses are standard errors. The asterisks denote coefficients that were significantly different from zero (corrected $p \leq 0.05$) after FDR correction.

		Thalamus	**BG**	**Midbrain**	**WM**
Apparent diameter	Intercept (mm)	0.71 (0.05)	0.84 (0.04)	0.63 (0.07)	0.69 (0.03)
	c_{gender} (mm)	0.013 (0.027)	0.002 (0.020)	0.094 (0.038)	0.015 (0.015)
	c_{age} (μm/y)	0.48 (1.24)	1.32 (0.92)	2.71 (1.72)	1.43 (0.70)
VF	Intercept (%)	0.05 (0.07)	0.23 (0.23)	0.12 (0.07)	0.33 (0.24)
	c_{gender} (%)	−0.03 (0.04)	−0.23 (0.13)	0.05 (0.04)	−0.04 (0.14)
	c_{age} (%/y)	0.003 (0.002)	0.029 (0.006)*	0.0003 (0.0018)	0.012 (0.006)
Count	Intercept	5.9 (4.1)	35.3 (8.7)	5.6 (2.0)	417 (145)
	c_{gender}	−2.1 (2.4)	−7.5 (5.0)	1.2 (1.2)	−34 (83)
	c_{age} (y^{-1})	0.19 (0.11)	0.89 (0.22)*	−0.01 (0.05)	7.32 (3.74)
rCNR	Intercept	22.6 (2.6)	28.5 (2.6)	26.4 (3.6)	22.4 (1.5)
	c_{gender}	0.89 (1.49)	−1.9 (1.5)	1.8 (2.0)	−1.1 (0.9)
	c_{age} (y^{-1})	0.10 (0.07)	0.14 (0.07)*	0.24 (0.09)*	0.09 (0.04)*

Author Manuscript

Author Manuscript

Author Manuscript

Author Manuscript

Table 5

Rows 2–5: residual coefficients of variation of the PVSV parameters after regressing out effects of age and gender in thalamus, BG, midbrain, and WM. Rows 6–9: R^2 of the linear regression analyses.

		Thalamus	BG	Midbrain	WM
Residual Coefficient of Variation	Apparent diameter	0.1	0.062	0.12	0.053
	VF	0.74	0.22	0.73	0.47
	Count	0.5	0.17	0.56	0.32
	rCNR	0.15	0.11	0.14	0.086
R square	Apparent diameter	0.01	0.057	0.19	0.12
	VF	0.082	0.46	0.052	0.11
	Count	0.11	0.36	0.031	0.11
	rCNR	0.066	0.17	0.17	0.18

Author Manuscript

Author Manuscript

Author Manuscript

Author Manuscript

Table 6

Group averaged (n = 22) apparent diameter, VF, count, and rCNR of PVSVs in the thalamus, BG, midbrain, and WM during air and carbogen breathing. In the four rows for each parameter, the first and second rows are the mean (standard deviation) values under air and carbogen breathing conditions, respectively. The third row gives the percent difference between carbogen and air. The fourth row gives the FDR corrected p values from the Wilcoxon's signed rank test of the null hypothesis that there is no difference in the PVSV parameter between the two gas conditions.

		Thalamus	**BG**	**Midbrain**	**WM**
Apparent diameter	Air	0.72 (0.08)	0.87 (0.04)	0.74 (0.10)	0.75 (0.04)
	Carbogen	0.73 (0.08)	0.88 (0.06)	0.75 (0.09)	0.76 (0.04)
	% difference	1.9 (7.2)	0.92 (4.1)	2.9 (18)	1.6 (2.4)
	Corrected p	0.45	0.45	0.59	0.0058
VF	Air	0.14 (0.13)	1.2 (0.44)	0.16 (0.11)	0.78 (0.4)
	Carbogen	0.14 (0.13)	1.2 (0.48)	0.17 (0.12)	0.85 (0.4)
	% difference	15 (32)	5.3 (9.9)	180 (830)	9.5 (11)
	Corrected p	0.15	0.0033	0.9	0.0033
Count	Air	12(7)	66 (15)	6.3 (3.6)	699 (235)
	Carbogen	12 (6)	68 (15)	6.7 (3.2)	732 (234)
	% difference	8 (30)	4 (9)	43 (60)	6 (11)
	Corrected p	0.62	0.15	0.62	0.15
rCNR	Air	27 (4)	33 (3)	36 (5)	26 (3)
	Carbogen	29 (5)	34 (4)	38 (7)	27 (3)
	% difference	7.1 (8.8)	4.6 (4)	4.1 (10)	3.5 (3.2)
	Corrected p	0.0011	0.00017	0.085	0.00024